UNIVERSITY OF OKLAHOMA

GRADUATE COLLEGE

CHARACTERIZING FERRIHYDRITE TRANSFORMATION PRODUCTS IN NEAR-SATURATED BRINE ENVIRONMENTS

A THESIS

SUBMITTED TO THE GRADUATE FACULTY

in partial fulfillment of the requirements for the

Degree of

MASTER OF SCIENCE

By

KAYDRA BARBRE

Norman, Oklahoma

2023

CHARACTERIZING FERRIHYDRITE TRANSFORMATION PRODUCTS IN NEAR-SATURATED BRINE ENVIRONMENTS

A THESIS APPROVED FOR THE
SCHOOL OF GEOSCIENCES

BY THE COMMITTEE CONSISTING OF

Dr. Megan Elwood Madden
Committee Chair

Dr. Andrew Elwood Madden

Dr. Caitlin Hodges

ACKNOWLEDGEMENTS

I would like to thank my committee members, Dr. Megan Elwood Madden, Dr. Andrew Elwood Madden, and Dr. Caitlin Hodges for their guidance and assistance through the course of this research project. I would also like to thank my critical zone geochemistry research group, in particular Katherine Sluder, Andrew Rodriguez, and Cansu Demirel Floyd, for their support in feedback and lab assistance. Thank you to my family, friends, and professors for their support and encouragement through the course of my research. This study was funded by the University of Oklahoma and NASA grant #80NSSC23K0

TABLE OF CONTENTS

LIST OF FIGURES

LIST OF TABLES

ABSTRACT

Ferrihydrite transformation pathways are critical in understanding iron cycling and mineral transformation processes in extraterrestrial systems such as those observed on Mars. While common throughout terrestrial near-surface environments, ferrihydrite is highly susceptible to transformation to more stable iron oxides like goethite and hematite via aqueous alteration. Data from Mars rover missions show ferrihydrite associated with significant salt deposits on Mars' surface. Previous studies have shown that salt compounds are ubiquitous on Mars' surface and likely formed from ancient and modern brines that strongly influence(d) mineral alteration. This study investigates the effects of brine chemistry on synthesized ferrihydrite alteration. Batch reaction experiments were conducted for 30 days with near-saturated brines (NaCl, $CaCl_2$, $MgCl_2$, $NaNO_3$, Na_2CO_3, Na_2SO_4, $NaClO_3$, $NaClO_4$, and $MgSO_4$) as well as ultra-pure water (UPW) as a control. We also investigated the effects of varying brine concentrations by using 1:2 and 1:10 diluted mixtures of the near-saturated brines. X-ray diffraction (XRD) and Raman spectroscopy showed that ferrihydrite was preserved in near-saturated solutions of $MgSO_4$, Na_2SO_4, and $NaClO_4$ and did not show evidence of dissolution/transformation, while ferrihydrite partially transformed into other iron oxide phase products in the remaining brines. We also compared the mineral reaction products between freeze-dried ferrihydrite and undried ferrihydrite slurry through a series of replicate experiments with NaCl, $NaNO_3$, $NaClO_4$, $MgSO_4$, and $MgCl_2$. The freeze-dried ferrihydrite produced significant differences in reaction products in XRD samples. Samples from the slurry batch showed greater abundance of goethite and hematite compared to the dried initial and replicate batches, indicating that particle size and/or drying history also has a significant effect on ferrihydrite stability and dissolution/transformation. Solubility of iron oxide products was low in

all the samples, despite varying pH conditions. Determining the iron oxide phases present in the samples required combining XRD and Raman analyses. Overall, ferrihydrite remained unaltered in higher sulfate and perchlorate concentrations. In the context of soils and regolith observed on Mars, ferrihydrite may be more likely to resist transformation to hematite and goethite when found in areas where these salts are dominant. Ferrihydrite preservation may also be more likely when the ferrihydrite has been desiccated in a cold, arid environment prior to exposure to brines.

INTRODUCTION

Iron cycling is an important, fundamental surface process in soil and regolith evolution, yet in the context of Mars, it is poorly understood. Iron oxides are ubiquitous on the surface of Mars, and their presence indicates past and potentially current aqueous alteration of iron-bearing minerals, which has recently been confirmed by Mars rover and satellite data collection (Dehouck et al., 2017). Amorphous nanophase ferric oxides constitute roughly 20% of amorphous content in Martian dust, as confirmed in Meridiani Planum by Mars Exploration Rover *Opportunity* and Jezero Crater by *Perseverance* (Berger et al., 2016; Day & Dorn, 2019; Lemmon et al., 2022). Ferrous iron is prevalent in the basaltic rocks that comprise the majority of the Martian crust. Dissolution and oxidation of these mafic igneous rocks and their sediments leads to the formation of ferric iron and precipitation of ferrihydrite, hematite, goethite, and other iron oxide phases (Bell et al., 2022; Berger et al., 2016; Dehouck et al., 2017). Studies investigating the effects of near-saturated brines on various iron-bearing minerals have been investigated extensively, and analysis of their transformation products finds that ferrihydrite frequently appears following dissolution of jarosite, siderite, and pyroxene (Cullen et al., 2021; Elwood Madden et al., 2012; Phillips-Lander et al., 2019; Pritchett et al., 2012). Despite the abundance of ferrihydrite detected in Mars soil and dust, its recurring association with abundant salt deposits, and reports of its formation in other mineral dissolution experiments, our understanding of ferrihydrite stability and preservation in near-saturated Mars-analog brines is lacking.

Ferrihydrite is a a common and abundant mineral phase where aqueous alteration occurs. However, it is also metastable and poorly crystalline, making it difficult to characterize. Iron oxide characterization and reactivity is more complex and nuanced in solutions with high

salinity, such as those found on past present-day Mars. New data from Mars rover and satellite missions have shown the importance of understanding the influence of near-saturated brines on iron-bearing minerals on Mars given the abundance of sulfate, chloride, and perchlorate salt deposits on the surface (Phillips-Lander et al., 2019; Sefton-Nash & Catling, 2008). Therefore, the stability and transformation pathways of ferrihydrite in Mars fluids may affect the presence and distribution of other more stable iron oxide phases in Mars soils and regolith. We focus on understanding 2-line ferrihydrite stability, alteration, and reaction products in experiments with nine near-saturated Mars-analog brines (NaCl, $MgCl_2$, $CaCl_2$, $NaNO_3$, Na_2CO_3, Na_2SO_4, $NaClO_3$, $NaClO_4$, $MgSO_4$) and ultrapure water (UPW). This study will contribute to a better understanding of ferrihydrite presence and stability in high salinity environments and contribute to our broader understanding of iron cycling on Mars, both in the past and present.

We hypothesize that sulfate ions in near-saturated brines are more likely to preserve ferrihydrite against dissolution for longer periods of time, given that sulfates appear with considerable abundance on Mars' surface, often in close association with ferrihydrite (Dehouck et al., 2017; Toner et al., 2014; Tosca & McLennan, 2006). Aqueous alteration has certainly occurred in the past as evidenced by the appearance of iron alteration products in martian nakhlites that includes salt-bearing veinlets with ages ranging from 175 Ma to 4.5 Ga (Leshin & Vicenzi, 2006). Ferrihydrite typically does not remain stable following burial, often less than 10,000 years; therefore, its appearance in rocks on Mars that are significantly older than 10,000 years suggests unique geochemical factors contributing to its preservation (Dehouck et al., 2017; Leshin & Vicenzi, 2006; Sidhu, 1981). The formation and presence of brines may explain this apparent contradiction, given that brines are already hypothesized to play a significant role in modern aqueous processes on Mars (Chevrier & Rivera-Valentin, 2012). Near-saturated brines

may form on modern Mars through deliquescence, evaporation, or ice-salt interactions leading to aqueous alteration (Rivera-Valentín et al., 2020). Their chemistry will therefore have a direct influence on the behavior and profile of mineralogical assemblages, notably with a mineral as thermodynamically unfavorable as ferrihydrite.

BACKGROUND

Ferrihydrite ($(Fe^{3+})_2O_3$•$5/9H_2O$) is often the first of several possible iron (oxyhydr)oxides to form as a result of the dissolution of Fe-bearing minerals and oxidation of Fe^{2+} (Bibring et al., 2007; Cornell & Schwertmann, 2003; Jiang et al., 2018) as ferrihydrite is a metastable secondary mineral and intermediate phase in the transformation from Fe^{2+}-minerals to iron oxides such as goethite and/or hematite. In soil sciences, ferrihydrite is of particular interest as a source of Fe^{3+} to microbial environments due to its high surface area and relative instability in terrestrial environments, making it an important component of iron cycling and availability (Liu et al., 2008). Other iron oxide phases such as schwertmannite, lepidocrocite, magnetite and akaganéite may form due to the suppression of goethite or hematite formation, and are dependent on the presence of different cations and anions present in the system from other surrounding minerals (Bibring et al., 2007; Cornell & Schwertmann, 2003; Glotch & Kraft, 2008). Lower activation energies and interfacial free energies also account for these phases forming prior to more thermodynamically stable goethite and hematite (Navrotsky et al., 2008; Sidhu, 1981). While phases such as schwertmannite, akaganéite, and magnetite may form depending on the geochemical conditions following ferrihydrite alteration, they still tend to be thermodynamically unfavorable and eventually undergo further alteration to form goethite and hematite (Burleson & Penn, 2006; Sidhu, 1981).

In general, Fe-bearing mineral transformations in aqueous systems are governed by a few important factors: the pH of the solvent, the temperature of the environment, and the presence of foreign cations and anions (Cornell & Schwertmann, 2003). These factors influence mineral transformation by promoting or hindering different stages of compound reassembling. Goethite and hematite constitute the bulk of dominant reaction products from crystallization of ferrihydrite in terrestrial settings but have considerably different formation mechanisms. Hematite tends to be favored in systems where T>80°C (Arinchtein et al., 2020; Das et al., 2011; Glotch & Kraft, 2008; Liu et al., 2008). Both phases represent an overall decrease in total surface area (Das et al., 2011) compared to ferrihydrite precursors, which often form as intermediate iron oxyhydroxide phases following primary mineral dissolution. Foreign ions in abundance with ferrihydrite are known to alter transformation rates and pathways even when dehydration of a system does not occur. In some cases, goethite nucleation may be suppressed when anions form complexes with the ferrihydrite mineral surface, and indirectly promote hematite and/or lepidocrocite formation over longer periods of time (Cornell & Schwertmann, 2003). The presence of Fe^{2+}(aq) also significantly impacts ferrihydrite dissolution/transformation rates, resulting in accelerated formation of goethite and/or precipitation of magnetite (Cornell & Schwertmann, 2003; Liu et al., 2008).

Various iron-bearing minerals have been detected on the martian surface via *in situ* Mössbauer spectrometery, X-ray diffraction (XRD), as well as OMEGA/Mars Express onboard imaging spectrometers in orbit investigating VNIR ranges of 0.35-5.1 μm (Bibring et al., 2007). Jarosite, ferrihydrite, and various other iron oxides have been observed on Mars, however these phases are usually considered ephemeral under Earth surface conditions and are not typically well-preserved in the terrestrial rock record. This leads researchers to hypothesize that Mars'

unique surface conditions, including the presence of abundant salts, is the primary cause for differences in the observed iron mineral assemblages (Barron et al., 2006; Brass, 1980; Mills et al., 2013). For example, previous rover missions have identified iron (III) oxides in Meridiani Planum, Gusev Crater, and Gale Crater in close association with sulfate deposits within low-albedo sands (Bibring et al., 2007; Golden et al., 2008; Mianping et al., 2013).

Recent data collected from the Mars 2020 rover *Perseverance* also shows that hydrated ferric oxides are pervasive at the Jezero Crater landing site (Bell et al., 2022). Among two regolith types identified at Jezero, ferric iron was most prevalent in redder, fine-grained regolith alongside other crystalline, hydrated alteration phases, and in crystalline and amorphous nanophases within Martian dust (Bell et al., 2022). Ferrous iron-bearing minerals pyroxene and olivine were observed in greater abundance within the darker, coarser-grained regolith. Crystalline and amorphous ferric oxides phases have been identified at Gale Crater, Meridiani Planum, Gusev Crater, and now Jezero crater, suggesting that aqueous alteration was active in Mars' geological past and may continue as an ongoing surface process (Bell et al., 2022; Dehouck et al., 2017; Mianping et al., 2013).

Salts are also a significant component of Martian regolith (Clark & Van Hart, 1980; Mianping et al., 2013; Thomas et al., 2019). Salts on Mars likely formed from several possible mechanisms: secondary concentrations of chemical weathering processes of which the movement of subsurface water plays an important role, the evaporation of surface water from ancient oceans/lakes leaving near-saturated salt brines behind, or the direct condensation of volatiles released from planetary processes such as volcanism (Clark & Van Hart, 1980; Osterloo et al., 2008). Based on the size and abundance of salt deposits detected by Mars landers and rovers *Viking*, *Spirit,* and *Opportunity,* large-scale evaporation of Mars' oceans and lakes

roughly ~3.5 billion years ago seems to be the likely explanation for these evaporite salts (Mianping et al., 2013; Osterloo et al., 2008; Thomas et al., 2019). Several salt groups have been identified as the dominant compounds in Martian regolith: chlorides, sulfates, bromides, carbonates, perchlorates, and nitrates. XRF analysis from *Viking 1* and *2* landers detected sulfate, chloride, carbonate, and bromide deposits, with sulfate salts being the dominant group in martian regolith (Mianping et al., 2013; Osterloo et al., 2008; Toner et al., 2014). Data collected on martian dust from *Curiosity* rover at Gale crater by Alpha-Particle X-ray Spectrometry (APXS) show a considerable concentration of sulfur and chloride that is positively correlated with total Fe content, particularly within amorphous components of both martian soil and dust (Berger et al., 2016). Their greater abundance compared to other oxides measured in martian dusts suggest that their presence is best explained by incorporation into polyatomic ions such as perchlorate and/or a more complex mixture of salt phases rather than a single salt phase (Berger et al., 2016; Sears & Chittenden, 2005).

Dense, near-saturated brines also lower the freezing point for H_2O (Möhlmann & Thomsen, 2011). Brines have long been hypothesized to exist on the martian surface resulting from deliquescence and/or melting of water ice by salts (Rivera-Valentín et al., 2020). Their stability on Mars' surface and within the subsurface is dependent on salt-water mixture stability against evaporation so that atmospheric water vapor pressure and water vapor pressure in the space just above the brine are nearly equal. Models show that brines with a eutectic temperature above 270 K are not stable under Mars atmospheric conditions, but are metastable between eutectic temperature T_E and 270 K (Rivera-Valentín et al., 2020). It is also at this range where deliquescence occurs. The same models found that the kinetics of deliquescence may be too slow to account for modern brine movement on Mars' surface, and suggest that salt-ice melting

interactions may be the preferred brine-forming process that accounts for brine formation and presence alongside topographical features such as recurring slope lineae (RSL) (Chevrier & Rivera-Valentin, 2012; Rivera-Valentín et al., 2020).

The salt composition or mixture that would account for the movement of modern subsurface water and ions is still being investigated, as perchlorates, chlorides, sulfates, and nitrates all have different degrees of effectiveness in matching eutectic points for conditions observed on Mars. Some compounds, such as $CaCl_2$, H_2SO_4, $FeCl_3$, and most nitrates are less likely to dominate brine assemblages due to their instability in the presence of sulfates and carbonates within the soil and atmosphere and chemical reactivity with basaltic materials in Martian soil (Clark & Van Hart, 1980). In terrestrial environments on Earth, carbonate salts tend to dominate as a result of higher volumes of brine with low salinity resulting in extensive carbonate mud, limestone, and dolostone deposits. In contrast, the notable lesser quantity of carbonate deposits on Mars may be a result of dissolution by volcanic acidic fluids which in turn contributed to the accumulation of CO_2 in the atmosphere (Mianping et al., 2013). The fact that sulfate and chloride salts have been detected in large deposits by XRF and APXS and the absence of abundant carbonates indicates large-scale evaporation of Mars' ancient oceans and loss of carbonate deposits from chemical weathering by acidic fluids (Cullen et al., 2021; Mianping et al., 2013). Researchers suggested that the most probable assemblage of brine composition is dominated by $MgSO_4$ and $Mg(ClO_4)_2$, with secondary components of Na_2SO_4, NaCl, and minor amounts of carbonates and bromides (Phillips-Lander et al., 2019; Rivera-Valentín et al., 2020; Toner et al., 2014). Based on data from Mars rover and satellite missions, perchlorate salts ($Na,Mg,Ca(ClO_4)_2$) have also been detected alongside sulfate salts and iron mineral outcrops and in association with RSL. while

carbonates are in very low abundance (Cullen et al., 2021; Legett et al., 2018; Rivera-Valentín et al., 2020).

Several studies have been conducted to determine the effects of near-saturated brines on iron-bearing mineral dissolution using sulfate, chloride, and perchlorate salts. Jarosite has received attention since its detection at Meridiani Planum, and its presence indicates that acidic fluids have acted on Mars' surface, if but for a short time (Pritchett et al., 2012; Zahrai et al., 2013). Jarosite is typically found in acid mine drainage sites in terrestrial environments at low pH conditions alongside an abundance of iron oxyhydroxides like ferrihydrite (Huminicki & Rimstidt, 2009). Findings from jarosite studies showed that near-saturated chloride brines significantly delayed the rate of jarosite dissolution, and prolonged particle lifetime by a few thousand years (Pritchett et al., 2012). Differences in specific mineral chemistry also have an impact on their stability, namely with Na-jarosite and K-jarosite where the former remained stable against dissolution for longer at lower temperatures and acidic pH (Zahrai et al., 2013). Transformation tended to accelerate with controlled temperature rise in solutions, and resulted in hematite as the dominant end product for pH<7; ferrihydrite was dominant in pH>7 with some minor maghemite (Elwood Madden et al., 2012). Siderite ($FeCO_3$) was also detected in salt outcrops, which surprised researchers given that carbonate salts were in minimal abundance on Mars, and found that this mineral dissolves quickly in acidic fluids regardless of salinity, potentially the same fluids that contributed to Fe^{2+} oxidation to Fe^{3+} and the production of jarosite (Cullen et al., 2021). Pyroxene dissolution experiments in near saturated chloride and sulfate brines also showed cases where dissolution and Fe-release rates increased with increasing salinity when pH was low (Phillips-Lander et al., 2019). Pyroxene dissolution led to the production of secondary clay minerals which have also been observed in association with brines.

In these studies where alteration products were analyzed after the selected starting mineral reacted with brines, Fe-(oxyhydr)oxide minerals (such as ferrihydrite) were identified as secondary alteration products. Ferrihydrite has been detected in outcrops at Gale Crater, Meridiani Planum, and Jezero Crater, and has been consistently identified in dissolution experiments as a secondary alteration product in jarosite, siderite, and pyroxene aqueous alteration. Analyzing its stability and transformation in Martian brines as a starting material warrants further investigation.

METHODS

Ferrihydrite was synthesized using a method modified from Cornell and Schwertmann 2003 which is based on the following reaction:

$$Fe(NO_3)_{3\,(aq)} + 3KOH_{(aq)} \rightarrow Fe(OH)_{3\,(s)} + 3KNO_{3\,(aq)}$$

We slowly added 1M KOH to 500 mL of 0.1M $Fe(NO_3)_3$ until the pH reached a value between 7-8, typically 170-190 mL per 500 mL 0.1M $Fe(NO_3)_3$ (See Table 1). Once we reached the target pH range, we centrifuged the mixture to separate the precipitate out of solution at 7500 rpm for five minutes, then we placed the precipitate in 6-8 kD dialysis tubing and dialyzed until conductivity reached 0. After dialysis, the slurry was frozen and dehydrated via freeze-drying to produce a powder for X-Ray Diffraction (XRD) and Raman analysis. This procedure was replicated six times to produce 25-30 g of 2-line ferrihydrite. XRD analysis confirmed that we synthesized 2-line ferrihydrite with poor crystallinity, with broad peaks at ~34° and ~61° 2θ using Cu Kα radiation (see Figure 1). Across all five batches, we synthesized 24.5 g of 2-line ferrihydrite. For the slurry replicate experiments, we omitted the freeze-drying step and added the dialyzed ferrihydrite slurry to the brine solutions directly to prevent particle aggregation.

We also synthesized 250 mL near saturated (NS) NaCl, $NaNO_3$, Na_2CO_3, Na_2SO_4, $NaClO_3$, $NaClO_4$, $CaCl_2$, $MgCl_2$, and $MgSO_4$ brines as well as 1:2 and 1:10 dilutions of the near-saturated solution to test the effects of varying salt concentration, in addition to one ultra-pure water (UPW) solution for a negative control, totaling 28 solutions of 250 mL. Near-saturated brines were synthesized by adding anhydrous salt to UPW at room temperature until no more salt could dissolve. Molar concentrations of these solutions differed based on the salt type, due to differences in solubility. Once synthesized, pH was measured for each brine type and concentration level of each brine dilution point in mol/kg H_2O (see Table 1).

Once we confirmed that the synthesized material was 2-line ferrihydrite via XRD, we added ~0.25 g of ferrihydrite to each 250 mL solution and sealed the mixture in a plastic bottle with parafilm around the screw-on cap to prevent leakage. All 28 solutions were placed in a New Brunswick™ Innova® 42 Series Incubator Shaker to mix at 150 rpm at 20°C for a period of 30 days. After 30 days of mixing, the brine solutions were vacuum filtered with 0.45 µm filter paper and acidified with 2-3 drops of 0.1M HNO_3 to prevent precipitation of new iron compounds from any dissolved iron present. Filtered iron oxide precipitates were frozen and freeze-dried prior to mineral analysis by XRD and Raman microscopy. We used XRD on a Rigaku Ultima IV diffractometer with a scintillation detector and curved graphite monochromator (Cu-Kα radiation, 40 kV, 44 mA) to identify the specific iron oxide phases present and relative quantities of each phase in the bulk sample. For XRD data analysis, we used MDI Jade analysis software with ICDD (International Centre for Diffraction Data) PDF4+ database. Raman spectra were collected using a Renishaw InVia High Resolution Mapping Raman Microscope with a 785 nm red laser. We collected spectra for 180 seconds at 0.1-0.5% power with a 1200 l/cm grating to further characterize individual iron oxide particles within each sample. Surface texture and

crystal habit were determined using Scanning Electron Microscopy (SEM). Filtered precipitates were treated with an Ir sputter-coating to reduce charging in a high vacuum chamber for SEM. We collected secondary electron imaging at a magnitude range of 5000-50,000x to determine particle shape and size, along with Energy Dispersive X-ray Spectroscopy to determine relative atomic and weight percentages of Fe and O. For further analysis of ferrihydrite particle size and crystallinity, we used a 200 kV JEOL 2000FX Transmission Electron Microscoe (TEM). Each sample was suspended in UPW and dispersed via sonication. The suspended sample was then dropped onto a lacey carbon copper TEM grid for analysis. Electron diffraction confirmed the poorly crystalline nature of synthesized 2-line ferrihydrite.

RESULTS

From the iron oxide phases identified, we were able to determine the effect of salt composition and concentration on ferrihydrite stability in brines, as well as characterize the crystallinity and surface texture of any transformation products. Our results showed ferrihydrite is most likely to be preserved in near-saturated solutions of $MgSO_4$, Na_2SO_4, and $NaClO_4$ without the formation of other mineral phases. However, this depended on the drying state in which ferrihydrite came in contact with these brines.

Effect of Freeze-drying

Producing a powder of 2-line ferrihydrite by Cornell and Schwertmann (2003) requires a final freeze-drying step in order to remove excess water from the ferrihydrite particles formed. We found that freeze-drying the ferrihydrite slurry caused a significant degree of product clumping and potential recrystallization. Under Raman spectroscopy, 2-line ferrihydrite is characterized by broad peaks at 710, 510, and 370 cm^{-1} (Das & Hendry, 2011; Hanesch, 2009;

Mazzetti & Thistlethwaite, 2002). The synthesized material for this study also exhibited broad Raman peaks at 360-370, 510, and 710 cm^{-1}. It was the issue of large aggregate clumping that we decided to create two sets of replicate samples following the initial batch series, one with ferrihydrite synthesized following the same procedure as the initial batch series and one with ferrihydrite prepared without the final freeze-drying step (see Figure 2). The first set is denoted as 'dried' ferrihydrite, and the second set is denoted as 'slurry' ferrihydrite. The undried, slurry ferrihydrite still exhibited the same Raman spectra as the dried variety, which doesn't appear to indicate recrystallization after freeze-drying. Reactions using the ferrihydrite slurry provided additional insight on the effect of particle aggregation and drying on mineral transformation, and contributed to better sample preparation for TEM analysis (see Figure 3).

Reaction Products by XRD

Like the XRD spectra for unreacted ferrihydrite, the reaction product XRD signals for most brine solutions samples were weak and broad. Reaction products from the first UPW batch reaction consisted primarily of goethite with minor amounts of hematite, magnetite, and residual unaltered ferrihydrite. No secondary iron oxide phases were detected in near-saturated solutions of $MgSO_4$, Na_2SO_4, and $NaClO_4$, 1:2 saturated solutions of $MgSO_4$ and Na_2SO_4, and 1:10 saturated Na_2SO_4 (see Figures 4-13, subfigures A). Broad peaks at d-spacings 2.56 and 1.37 (Cu tube) were seen throughout most reaction products, however the abundance of noise made it difficult to determine additional iron oxide phases using the XRD patterns. Selecting out apparent peaks via inspection rather than the software-based algorithms used for phase identification, as the data were too noisy for statistically meaningful peak-search algorithms to work. Goethite, hematite, and lepidocrocite were the most common secondary XRD phases detected throughout solutions where ferrihydrite was not completely preserved, noted by smaller

peaks at 3.81 and 2.72 for goethite, 2.56 for hematite, and 3.24-3.12 for lepidocrocite. These were identified in solutions of UPW, all $NaNO_3$ solutions, and all Na_2CO_3 solutions (with greatest abundance in near-saturated and 1:2 diluted solutions). Akaganéite appeared in 1:2 diluted NaCl, near-saturated $CaCl_2$, 1:2 diluted $MgCl_2$, all $NaClO_3$, and 1:2 diluted $NaClO_4$ with peaks identified at 7.34-5.87 and 2.22. Korshunovskite [$Mg_2Cl(OH)_3 \bullet 4H_2O$] formed in $MgCl_2$ solutions and in greatest abundance in the near-saturated solution, and was more easily identifiable via Jade software analysis (see Figure 7a). Schwertmannite only appeared in 1:10 saturated $MgSO_4$ with peaks at 9.8 and 8.01, and akaganéite appeared secondary in near-saturated $CaCl_2$ and in minor amounts in $NaClO_3$. See Table 3 for results by wt% determined by whole-pattern fitting with MDI Jade software.

Based on the results from the initial batch series, we selected UPW, NaCl, $NaNO_3$, $NaClO_4$, $MgCl_2$, and $MgSO_4$ as solutions to revisit for replication experiments. The XRD results between the initial and slurry replicate batches showed interesting differences across brine concentrations and between dried and slurry replicate samples. UPW experiments with ferrihydrite slurry showed phase variation more similar to that of the first batch, but with considerably more hematite, as confirmed as the dominant phase based on Raman spectroscopy. Goethite was the dominant phase in the dried replicate sample, with ferrihydrite as the residual phase with minor amounts of lepidocrocite, hematite, and maghemite. Based on XRD data, few replicate samples showed consistent trends in reaction product phases between both the initial and replicate dried ferrihydrite samples, and the dried vs. slurry replicate samples. Near-saturated $MgSO_4$ still preserved ferrihydrite for the dried replicate sample, but the slurry sample yielded a greater amount of goethite with minor amounts of hematite, lepidocrocite, and maghemite. Both goethite and hematite occurred in more frequent and greater abundances in both replicate series

than the initial series. Korshunovskite appeared in $MgCl_2$ solutions again; 1:10 saturated solutions with both dried and slurry ferrihydrite registered the greatest abundance. Among the replicated series, only 1:2 and 1:10 saturated $MgCl_2$ solutions showed similar trends between dried vs. slurry ferrihydrite (see Table 3).

Reaction Products by Raman Spectroscopy

Like XRD spectra, Raman spectra were generally broad and noisy, likely due to the low laser power required to ensure we did not dehydrate or alter the sample. Ferrihydrite is susceptible to thermal alteration at laser power higher than 5%, and converts to hematite at power exceeding that level (Mazzetti & Thistlethwaite, 2002). Throughout the initial and dried replicate batch series, ferrihydrite was the dominant phase observed in most samples (Figures 4-13, subfigures b). Goethite and lepidocrocite appeared as the most common secondary phases. Only near-saturated $MgCl_2$ and 1:2 saturated $MgCl_2$ and $NaNO_3$ did not have ferrihydrite as the dominant iron oxide phase present, where goethite and lepidocrocite tended to dominate. These solutions also had the most iron oxide variety of the initial batch reaction solutions. Raman results for the dried replicate batch series were similar to the initial experimental set, with ferrihydrite still registering as dominant. However, hematite was the more common secondary iron oxide phase throughout all the solutions of the freeze-dried replicate set.

Goethite, lepidocrocite, and hematite appeared more frequently in ferrihydrite slurry reaction batch samples compared to the initial and dried replicate batch series. Minor peaks from maghemite and schwertmannite also appeared in 1:2 saturated $MgSO_4$, and maghemite appeared more frequently in various concentrations of other brines. Ferrihydrite was dominant in less than half of UPW and brine solutions in the slurry batch. Korshunovskite appeared dominant or

secondary in initial and both replicate batches of 1:2 and near-saturated $MgCl_2$ solutions. See Table 4 for Raman identification results of initial and dried/slurry replicate samples.

Salt peaks appeared in several brine solutions, ranging from weak to strong intensity. This was likely due to residual salt left on the surface of ferrihydrite grains that did not fully wash off during vacuum filtration. With this consideration in mind, we excluded peaks associated with CO_3^{2-} (1064 cm^{-1}), NO_3^{2-} (1049 cm^{-1}), SO_4^{2-} (980 cm^{-1}), ClO_3^- (930 cm^{-1}), and ClO_4^- (928 cm^{-1}) from iron oxide mineral identification.

Scanning Electron Microscopy (SEM)

The first experimental trial with freeze dried ferrihydrite showed the degree to which particle clumping affected size distribution. Most samples showed grains ranging from a few nanometers to 500 μm in diameter. These grains were blocky and irregular in shape, with very little evidence of new particle formation in most samples (see Figure 14). Some larger grains also appeared to have dried precipitates of salt along edges and uneven surface textures within nearly all samples. This provides some explanation in regards to the strong salt peaks that appear in nearly all Raman spectra of near-saturated brines. Some samples showed evidence of spherical particles roughly 5nm in diameter at a magnification of 25,000x, namely in the samples from near-saturated NaCl, $NaNO_3$, and $MgSO_4$, and 1:10 Na_2SO_4 and $MgSO_4$ (see Figure 15). These particles were generally smooth and found on the surfaces of larger ferrihydrite grains. The sample from 1:10 diluted $NaNO_3$ also showed a long, prismatic-like particle on the surface of larger ferrihydrite grains (see Figure 16). The particle shape of these grains was not enough to determine individual mineral phases, but it does give some indication of new particle development within these brines. Since all of the samples are composed almost entirely of iron

oxides, Energy X-ray Dispersive Spectroscopy (EDS) did not offer additional constructive data for these mineral phases.

Only the ferrihydrite slurry replicate batch was analyzed by SEM for the replicate batch series. Ferrihydrite grains from this series were smaller in size compared to the first batch, diameters of 100 μm or less (see Figure 17). Surface textures of reacted ferrihydrite slurry were more uneven and chaotic compared to the freeze-dried batch. Apparent dissolution pits could be observed in a $NaNO_3$, $NaClO_4$, and UPW experiments, independent of concentration. Near-saturated $MgSO_4$ showed the most surface alteration compared to lower saturations (see Figure 18). Reaction products from 1:2 and near-saturated $MgCl_2$ experiments showed significant surface dissolution on ferrihydrite grains, as well as abundant formation of korshunovskite (see Figure 19). Several oblong aggregates were also observed in 1:2 saturated $MgCl_2$ sample, and in smaller quantities in near-saturated $MgCl_2$ and 1:2 saturated $NaNO_3$ samples (see Figure 20). These resembled some of the spherical particles observed in the previously mentioned solutions from the initial batch series but were significantly larger by comparison (30-50 μm). EDS analysis of these aggregates in $MgCl_2$ solutions showed that Fe, O, Mg, and Cl were the primary elemental components, indicating they contained a collection of iron oxides and korshunovskite. They were likely the result of smaller iron oxide slurry aggregates collecting and accumulating with korshunovskite while being mixed over the experimental trial period, hence the rounded shape.

Transmission Electron Microscopy (TEM)

Due to the issues of clumping from freeze-drying the initial ferrihydrite starting material, preparing the first experimental trial samples for TEM analysis proved difficult. The previously mentioned particle size range for freeze-dried ferrihydrite was too large for adequate suspension

in solution and placement on the copper grids, and were generally too thick for the electron beam to penetrate for imaging. The replicated ferrihydrite slurry was the more ideal form to create reaction products for observation (Figure 21), and it was for this reason we chose to select samples to image from the slurry replicate series. Electron diffraction patterns collected from unaltered ferrihydrite slurry particles also confirmed the poor crystallinity of our synthetic material.

Two samples were chosen from this set due to their interesting results observed in Raman and SEM: 1:2 and near-saturated $MgCl_2$. These samples bore a strong resemblance to the unreacted ferrihydrite slurry (Figure 22). Despite the higher detection of goethite, hematite, and korshunovskite in both of these samples, it was difficult to observe these phases through TEM. Figure 22b does have some appearance of small, needle-like structures intermixed within ferrihydrite slurry, which could potentially be korshunovskite. Figure 22d shows what does appear to be a semi-rectangular particle roughly 200 nm in length. In general, samples from these solutions were still clumped together when deposited on the copper grids. Additional phases formed may have been concealed within these clumps, making it more difficult to observe them through the varying thickness of individual aggregates.

Changes in pH

Different brine types and concentrations showed various changes in pH before and after reacting with ferrihydrite for 30 days (see Table 5). Most brine solutions in the initial batch reaction series were circumneutral (pH 5-8) before and after, with pH changes ranging -3.04 – 3.06 ± 1.49. All three solutions of Na_2CO_3 had an initial and final pH above pH 11, with very little change in pH. All three concentrations of $MgSO_4$ and NaCl started at a basic pH and decreased to slightly acidic or near-neutral. All three concentrations of $NaNO_3$ and $NaClO_3$

increased from slightly acidic to basic, and $NaClO_4$ experiments increased from slightly basic/near-neutral to basic pH. Changes in pH trends were not always consistent within the same brine type as concentration decreased. For example, the 1:10 diluted $CaCl_2$ solution increased from slightly acidic to slightly basic, while the 1:2 saturated solution decreased in pH while remaining acidic, and the near-saturated solution increased slightly while remaining acidic. The pH of the 1:10 diluted $MgCl_2$ solution decreased while remaining at a basic pH range, while the 1:2 saturated solution increased from slightly acidic to slightly basic, and the near-saturated solution remained slightly acidic with little change.

UPW solutions showed the most consistency between the initial batch reaction series and replicate series. The initial pH values for the initial, dried replicate, and slurry replicate were ~6 prior to adding ferrihydrite, then decreased to 4.56, 3.91, and 4.83 respectively. For the replicated brine solutions, some of the same pH trends were observed in both dried and slurry solutions (see Tables 6 and 7). All concentrations of $MgSO_4$ for both replicate series decreased from basic to slightly acidic/near-neutral. Overall, 59% of replicate solutions became more acidic, 34% remained relatively unchanged, and 7% became more basic.

DISCUSSION

Due to the poor crystallinity of ferrihydrite, characterizing our reacted samples with XRD proved challenging. 2-line ferrihydrite is the first phase to begin crystallizing out of many low-temperature aqueous solutions containing ferric iron. As such, its crystallinity tends to be poor compared to goethite and hematite which generally have longer-range order, greater thermodynamic stability, and therefore lower solubility. The ferrihydrite crystalline structure is very difficult to characterize even through reliable analytical methods, which explains why XRD scans were broad and produced significant background noise (Cudennec & Lecerf, 2006).

Dehouck et al (2017) stated that freeze-drying 2-line ferrihydrite slurry can cause partial recrystallization to 3-line ferrihydrite. Because of these conditions, the Jade software utilized for analyzing XRD data had difficulty distinguishing actual 'peaks' due to iron oxide phases from background noise; nanocrystalline diffracting domains and/or lack of long range order lead to very broad features. Additionally, the Cu X-ray tube in our diffractometer produces fluorescent X-rays in iron-bearing minerals, increasing background noise and obscuring diffraction-related signals. Results from Jade interpretation of XRD data were not always consistent with data obtained from Raman spectroscopy, including samples where magnetite was interpreted as the dominant Fe-oxide phase in XRD but no magnetite was detected in Raman. Although generally XRD is considered a more reliable method for determining crystalline mineral phases, using XRD to characterize ferrihydrite and its reaction products was challenging. While the results from XRD analysis can give a general interpretation of some iron oxide phases present within our samples, the calculated wt% of phases in each sample likely has a margin of error too large for exact calculations to be acceptable. In general, this corroborates SEM observations that micron-sized reaction products generally did not form in any experiments, which should have been readily detectable. While we cannot rely on the quantitative aspect of XRD data in this case, it is still beneficial in confirming the presence of secondary iron oxide phases when combined with Raman spectroscopy. Within this study, reliance on Raman spectroscopy for transformation product detection is much more reliable than XRD.

We initially hypothesized that sulfate brines would most effectively preserve ferrihydrite at near-saturated brine levels in the batch reactor series based on the observation of strong association of ferrihydrite with sulfate deposits on Mars. Our results from the initial and dried replicate batches support this hypothesis as ferrihydrite remained the only phase detected by

XRD and Raman in near-saturated $MgSO_4$ and Na_2SO_4. Ferrihydrite also remained stable in 1:2 and 1:10 saturated Na_2SO_4 and $NaClO_4$ solutions, potentially as a result of SO_4^{2-} and ClO_4^- absorbing on the surface of ferrihydrite grains and suppressing Fe-release and subsequent formation of other iron oxides or due to lower water activities (Cornell & Schwertmann, 2003; Legett et al., 2018). NaCl showed ferrihydrite preserved in the initial near-saturated solution, but the dried replicate experimental set showed the presence of additional iron oxide phases like hematite. UPW solutions from initial and replicate batches showed more diverse variation in iron oxide phases present, with goethite and hematite usually dominating with minor lepidocrocite, and a smaller amount of ferrihydrite remaining unreacted in solution. In the initial experimental set, $NaNO_3$, Na_2CO_3, $NaClO_3$, and $CaCl_2$ exhibited more variation in transformation products across differing concentration, with $NaNO_3$ and $CaCl_2$ solutions showing decreased diversity in reaction products as concentrations increased, and Na_2CO_3 and $NaClO_3$ solutions showing increased diversity as concentration increased. Effect of NO_3 and Cl on ferrihydrite transformation is reported to be smaller compared to polyvalent anions, which may offer an explanation for this trend (Cornell & Schwertmann, 2003). The detection of magnetite that occurred in some samples in XRD was likely due to the challenges of Jade software interpreting background noise as peaks indicative of magnetite presence, since Raman analysis did not confirm magnetite in most samples. Only very minor magnetite was detected in the UPW replicate solution with dried ferrihydrite.

We also observed significant differences resulting from the drying process, perhaps due to ferrihydrite aggregate sizes. Ferrihydrite aggregates from the synthetic slurry batch were significantly smaller compared to dried ferrihydrite where clumping occurred. Among slurry samples mixed with near-saturated and diluted brines, there was a significant change in

abundance of hematite, goethite, and lepidocrocite. Very few replicated brines from this set followed similar trends compared to the initial or dried replicate series. The surfaces of slurry particles were also more chaotic from reacting with brine solutions, as evidenced by rougher surfaces and dissolution pits observed in SEM. Previous observations of 2-line ferrihydrite slurry versus freeze-dried samples in resin embedded ultrathin slices via TEM demonstrate the freeze-drying results in irreversible internal rearrangement and recrystallization that produces domains with 10's of nm of longer-range order (Grefflé et al, 2001). This indicates that aggregate size and interaggregate structure is a more significant factor in ferrihydrite stability against dissolution than previously discussed, and may be in connection with surface area exposed to solutions during mixing. Previous studies in the context of terrestrial systems found that structural changes become more impactful on surface reactivity for iron oxides when approaching nanoparticle size due to expansion of unit cell parameters, which appear to support this theory (Heaney et al., 2020).

Since we did not buffer the pH of the brine solutions in this study, addition of ferrihydrite to brine solutions often had an impact on acidity and alkalinity. However, there was no clear trend linking pH change with ferrihydrite preservation or the nature of the reaction products. Indeed, changes in pH occurred even when no secondary iron oxide phases formed (e.g. near-saturated $MgSO_4$ became more acidic after mixing). Appearance of secondary iron oxides was also not restricted to solutions that only became more acidic or alkaline (e.g. UPW solutions decreased in pH while 1:10 saturated $NaNO_3$ solutions tended to increase, but both show diverse transformation product profiles). Interactions of salt anions on ferrihydrite particle surfaces may serve as a mechanism for hydrolysis that releases H^+ and OH^- depending on the initial conditions

of the brine solution and how anions adsorb on the ferrihydrite surface (Cornell & Schwertmann, 2003).

$$Fe(H_2O)_6^{3+} \rightarrow FeOOH\ +\ 3H^+ + 4H_2O$$

$$2Fe(H_2O)_6^{3+} \rightarrow Fe_2O_3 +\ 6H^+ + 9H_2O$$

The appearance of korshunovskite in our $MgCl_2$ samples was a surprise. Previous studies investigating mineral dissolution in $MgCl_2$ solutions did not report Korshunovskite forming among reaction products of iron-bearing minerals, and current data from Mars rover and satellite missions do not mention it as a mineral present in Mars deposits. Korshunovskite was first identified in the Korshunovskoye iron mine in Russia, thus giving it its name, and was found in association with magnetite and dolomite veinlets (Malinko, 1983). The presence of dolomite at this locality suggests this area was an ancient shallow marine environment. Korshunovskite appeared more abundant in solutions where pH decreased from alkaline/near-neutral to acidic or remained acidic. The lack of additional phases present in near-saturated samples indicates that ferrihydrite remained as korshunovskite formed. Ferrihydrite therefore may have acted as a catalyst for korshunovskite formation due to its iron abundance, and korshunovskite may only appear in O_2-rich environments with an abundance of Mg and Cl for formation and iron as a catalyst based on the conditions of its formation from this experiment. The lack of korshunovskite detected on Mars may indicate an absence of $MgCl_2$ salts and/or dissolved oxygen available to form this mineral structure, or simply that investigation into this mineral has not been considered.

Even when attempting to maintain consistent experimental conditions in our replicate batch series, reaction product trends still varied with small, unanticipated changes. Ferrihydrite

transformation appears to be more erratic when occurring at ~298K as opposed to results of similar experiments conducted at higher temperatures (>323K, e.g.) (Cornell & Schwertmann, 2003; Sears & Chittenden, 2005). Effects of foreign compounds on ferrihydrite stability and transformation are strongest at room temperatures due to complexing ligands, and this effect begins to decrease as temperature rises (Cornell & Schwertmann, 2003). Variations in the slurry replicate batches may be better explained by the differences in aggregate size, but hematite appeared more frequently in the dried replicate batch than the initial dried batch where goethite and lepidocrocite appeared more frequently. The internal organization that occurs during freeze-drying may have changed the nanoporosity inside aggregates, such that the size and charge of individual cations and anions in brines interacted differently with the 10's of nm domains present within the aggregates that were themselves tens to hundreds of microns (10,000 to 100,000s of nm) (Grefflé et al, 2001). The dried replicate series was kept at the same temperature and RPM during mixing as the initial batch and utilized the same container types and equipment. It appears that experimental variables not considered or out of our experimental control, though it is unclear as to which variables exactly, may be the cause for these discrepancies in our results at room temperature. For future studies determining transformation products, simulating temperature conditions closer to what is observed on Mars may provide a more accurate depiction of what would occur in Mars soil and regolith. We would anticipate greater production of hematite in high temperature experiments, and based on previous studies and the results of this study, ferrihydrite stability may be better reinforced at low temperature conditions (<273K).

The decision to add ferrihydrite slurry to brine solutions without removing excess water may have also affected the water/sample ratio compared to the dried samples. Dehouck et al, (2017) found that ferrihydrite preservation is also impacted by water/rock interactions, and may

be more likely to remain preserved in rock-dominated environments where water/rock ratio is lower. We attempted to maintain consistency of 250 mL of brine solution to 0.25g of sample for each batch, The addition of excess water from ferrihydrite slurry amounted to roughly 0.5-1 mL, but it is unlikely this would be enough to disrupt the consistency of our methods.

The differences observed between the two types of ferrihydrite starting material may also be indicative of ancient atmospheric patterns in Mars' geological history. Ferrihydrite that was frozen, then dried maintained better preservation after exposure to near-saturated brines, as opposed to ferrihydrite slurry which had been continuously wet from formation to exposure to brines and did not remain well preserved. Researchers have debated the evolution of Mars' cold and arid environmental conditions. Cold and arid conditions may have developed quickly early in Mars history and brines developed and caused subsequent aqueous alteration (Rivera-Valentín et al., 2020). Others argue that Mars maintained a warm and wet environment that gradually progressed to colder, drier conditions as liquid water became unstable over time (Mianping et al., 2013). Freeze-dried ferrihydrite may represent the former condition, drying prior to brine exposure, and ferrihydrite slurry may represent the latter, still containing liquid water when exposed to brines. Given the abundance of ferrihydrite and x-ray amorphous iron oxide nanophases detected by Mars rovers, our results appear to align better with the former hypothesis, that Mars developed cold and arid atmospheric conditions earlier in its history and ferrihydrite formation following aqueous alteration of iron-bearing minerals led to a freeze-drying effect that stabilized ferrihydrite in the presence of near-saturated brines.

When developing a system for predicting ferrihydrite stability and phase transformation in varying brine chemistries, we relied more on the results collected via Raman spectroscopy and XRD peaks identifiable via visual inspection of XRD spectra of freeze-dried experiments (see

Figure 23). Assuming ferrihydrite forms on Mars following the dissolution and oxidation of Fe^{2+}-bearing minerals, the effects of cations on ferrihydrite preservation is followed by Ca^{2+}< Mg^{2+}< Na^{+}, where ferrihydrite was most likely to be preserved in Na-bearing brines. In Cl^{-}-bearing solutions including chlorate and perchlorate, akaganéite forms as an intermediate phase to lepidocrocite. In lower concentrations of $MgSO_4$, schwertmannite likely forms as an intermediate phase to goethite, which was not observed in Na_2SO_4 and thus suggest the effect of Na^{+} is greater on ferrihydrite preservation compared to Mg^{2+}. NO_3^{-} and CO_3^{-} solutions exhibit the greatest effect of ferrihydrite transformation and are least effective at preserving ferrihydrite in dried conditions. Lepidocrocite, maghemite, goethite, and hematite appear at both low and high concentrations of these solutions, and with time are more likely to transform any remaining ferrihydrite to more thermodynamically stable iron oxides.

CONCLUSION

Aqueous alteration of ferrihydrite in near-saturated brines varies significantly between differing anion chemistries, with potential prolonged stability in sulfate and perchlorate brines where dissolution is prevented by mineral-anion interactions. Ferrihydrite detected on Mars' surface may therefore be in greater abundance where these salts are dominant. In greater concentrations of chloride, carbonate, and nitrate salts, hematite and lepidocrocite start to appear. As the concentration of these brines decreases, hematite and goethite start to form, along with minor amounts of maghemite, lepidocrocite, and schwertmannite.

Use of XRD and Jade software for determining phases present andtheir wt% proved to be less reliable than we originally anticipated due to the nature of 2-line ferrihydrite crystallinity, but does prove beneficial in identifying unexpected reaction products like Korshunovskite. A combined approach to mineral identification with XRD and Raman spectroscopy proves to be a

better approach. Aggregate size has a more significant role in ferrihydrite stability than previously discussed, and smaller aggregates appear less likely to remain stable regardless of high concentration and salinity. Transformation products become less predictable with smaller ferrihydrite aggregates, and ferrihydrite dissolution/transformation in sulfate and perchlorate salts may still occur. Distribution and stability of ferrihydrite may be predicated on the nature of aggregation in Mars soils and regolith alongside brine chemistry. Due to the dominance of sulfate/perchlorate salts on Mars, iron oxide phase profiles may contain greater abundances of ferrihydrite for longer periods of time compared to terrestrial environments on Earth.

FIGURES AND TABLES

Figure 1: XRD Results for Unaltered Ferrihydrite

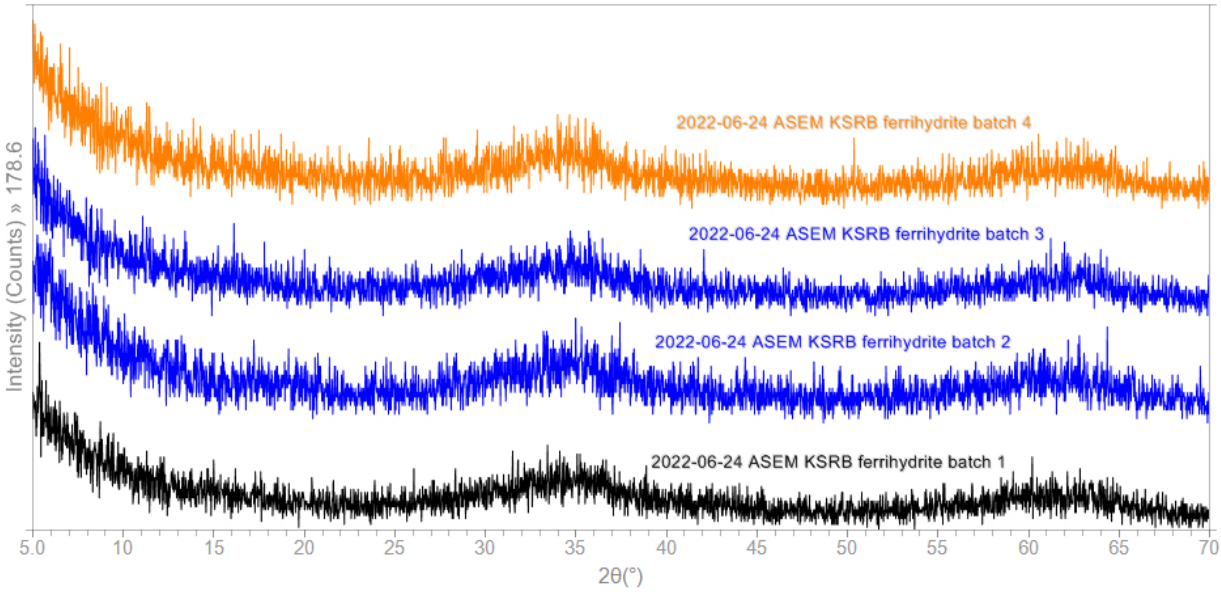

Figure 1: 2-line ferrihydrite is confirmed by two broad peaks at ~34° and ~61° in the XRD patterns. The broad peaks indicated very poor crystallinity and were consistent throughout all synthesized ferrihydrite batches.

Table 1: Brine Concentrations

Brine Type	Saturation	Concentration (mol/kg H_2O)	pH
NaCl	1:10	0.616	8.82
	1:2	3.080	9.03
	Near-sat	6.160	9.22
$NaNO_3$	1:10	1.073	6.10
	1:2	5.365	5.87
	Near-sat	10.730	5.78
Na_2SO_4	1:10	0.242	8.15
	1:2	1.074	8.30
	Near-sat	2.418	8.71
$NaClO_3$	1:10	0.198	6.18
	1:2	0.989	6.12
	Near-sat	1.978	6.51
$NaClO_4$	1:10	0.939	7.62
	1:2	4.696	7.96
	Near-sat	9.392	8.26
Na_2CO_3	1:10	1.672	11.53
	1:2	8.360	11.39
	Near-sat	16.720	11.30
$CaCl_2$	1:10	0.583	4.54
	1:2	2.915	5.56
	Near-sat	5.830	6.50
$MgCl_2$	1:10	0.570	9.37
	1:2	2.852	6.71
	Near-sat	5.703	6.17
$MgSO_4$	1:10	0.292	8.55
	1:2	1.458	8.25
	Near-sat	2.916	7.58

Table 1: Synthesized brine solutions listed with their saturation level (1:10, 1:2, and 'near-sat'), concentration in mol/kg H_2O, and pH for each solution. Most solutions were either acidic at all concentrations or basic, with the exception of $MgCl_2$ which was acidic at 50% and near-saturation and basic at 10% saturation.

Figure 2: XRD Results for Dried vs. Slurry Ferrihydrite

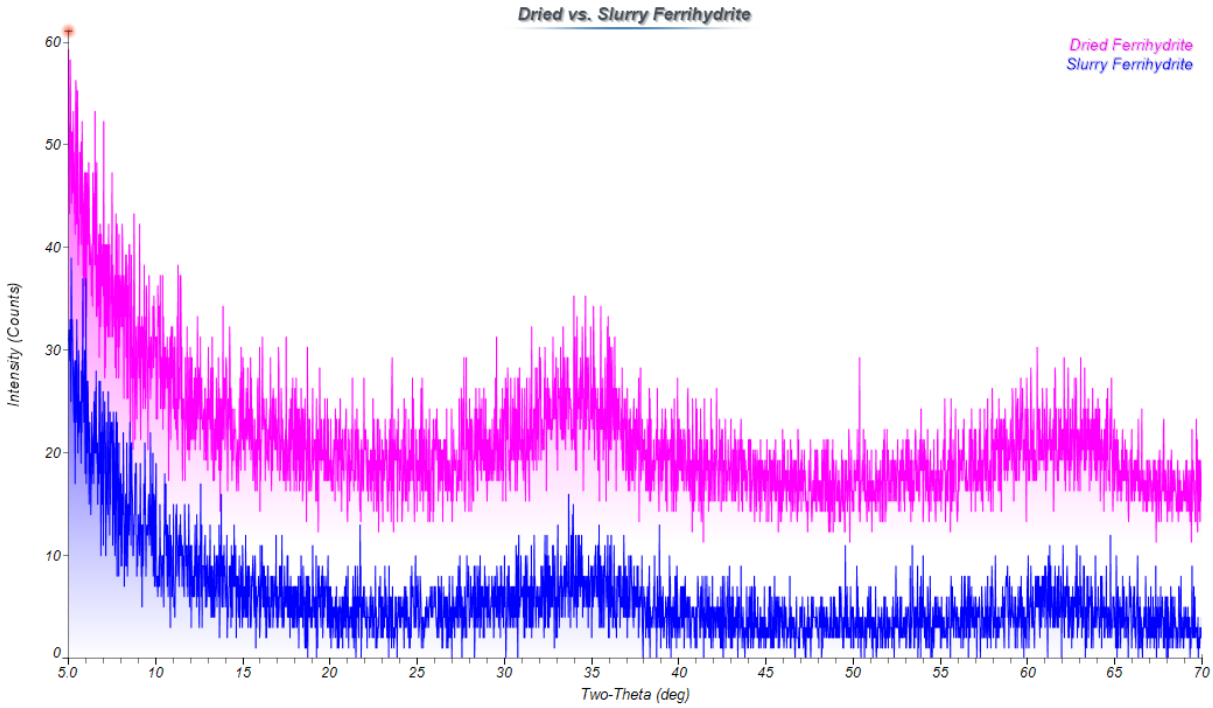

Figure 2: XRD spectra comparison between freeze-dried ferrihydrite (top) and ferrihydrite slurry (bottom). Both show noisy, broad peaks at ~34° and ~61°.

Figure 3: Images of Filtered Initial and Replicate Batches Post-Mixing

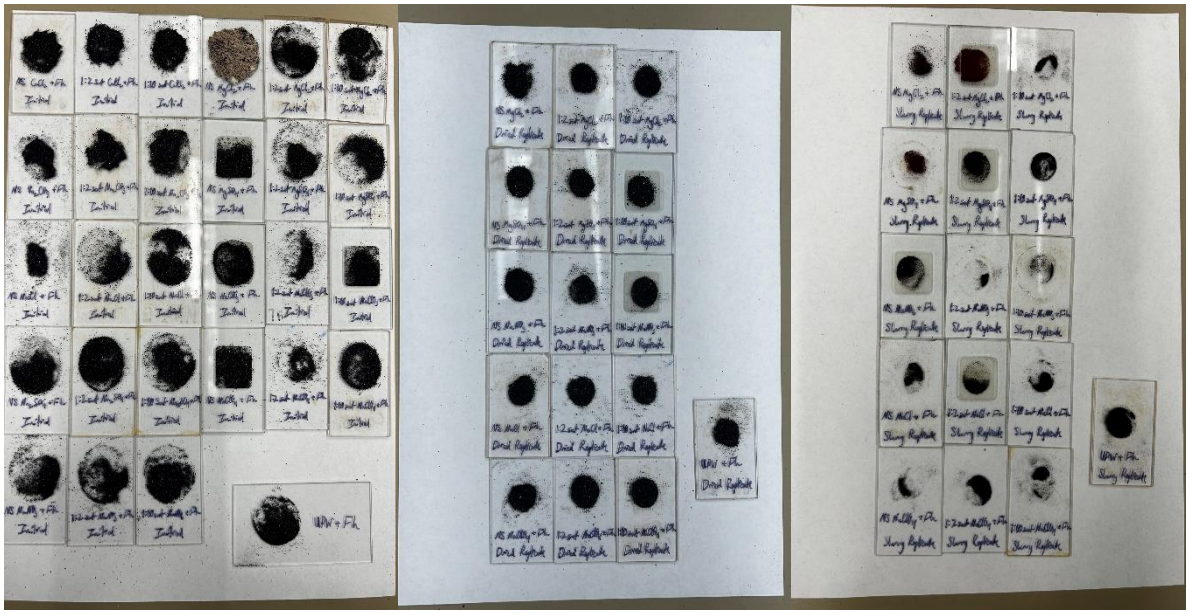

Figure 3: Pictures of filtered sample from the initial (left), dried replicate (middle), and slurry replicate (right) batches.

Figure 4: XRD and Raman Spectra for UPW Samples

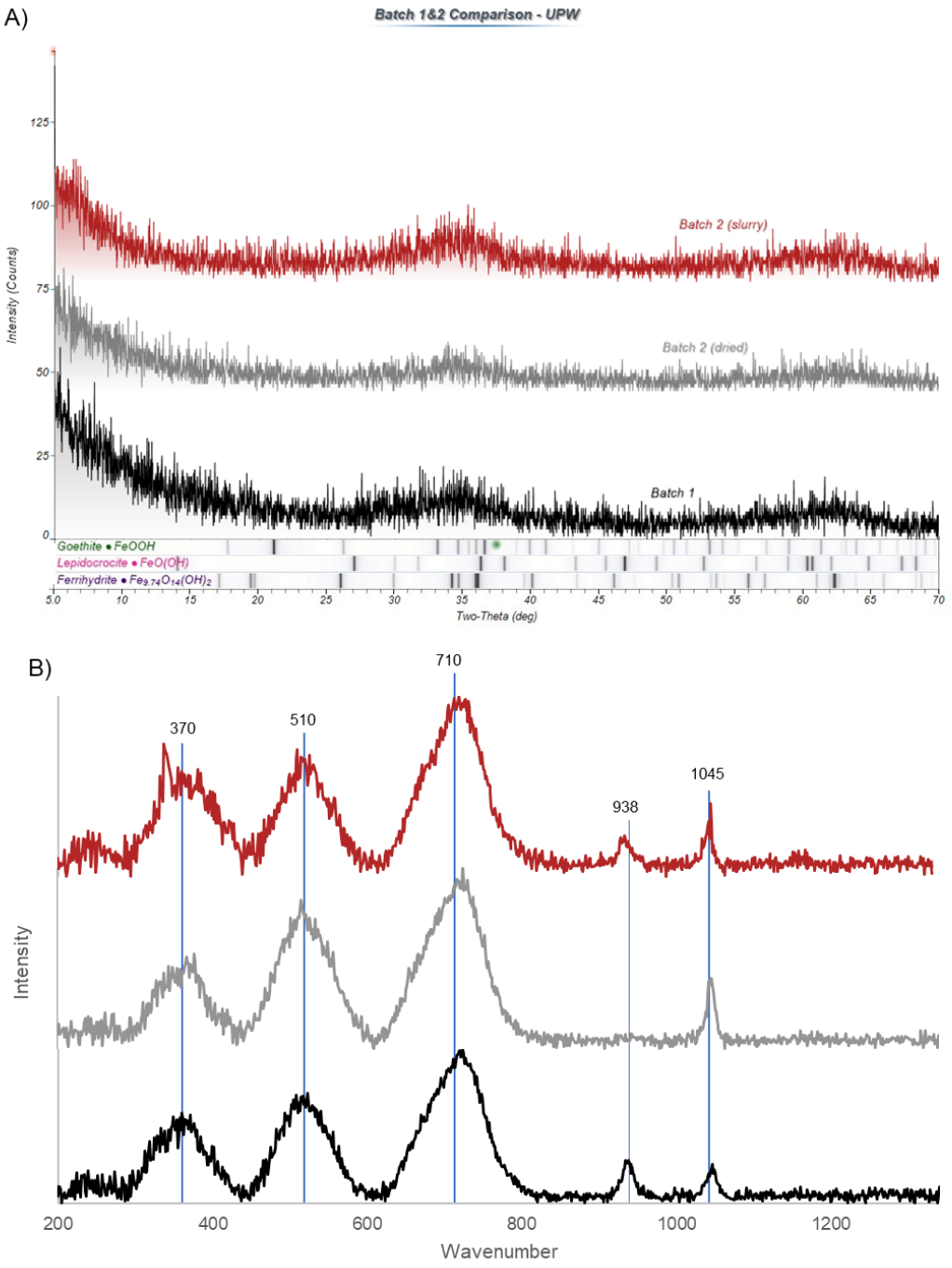

Figure 4: XRD (a) and Raman Spectra (b) for ultrapure water (UPW) solutions for initial (black), dried replicate (gray), and slurry replicate (red) samples. Values for peaks in Raman spectra are given in cm^{-1}. Broad XRD peaks at d-spacings 2.56 and 1.37 are indicative of 2-line ferrihydrite Raman peaks at 370, 510, 710, and 1045 are indicative of ferrihydrite (Das & Hendry, 2011), however the 938 peak does not appear to coincide with any known iron oxide phases.

Figure 5: XRD and Raman Spectra for NaCl Samples

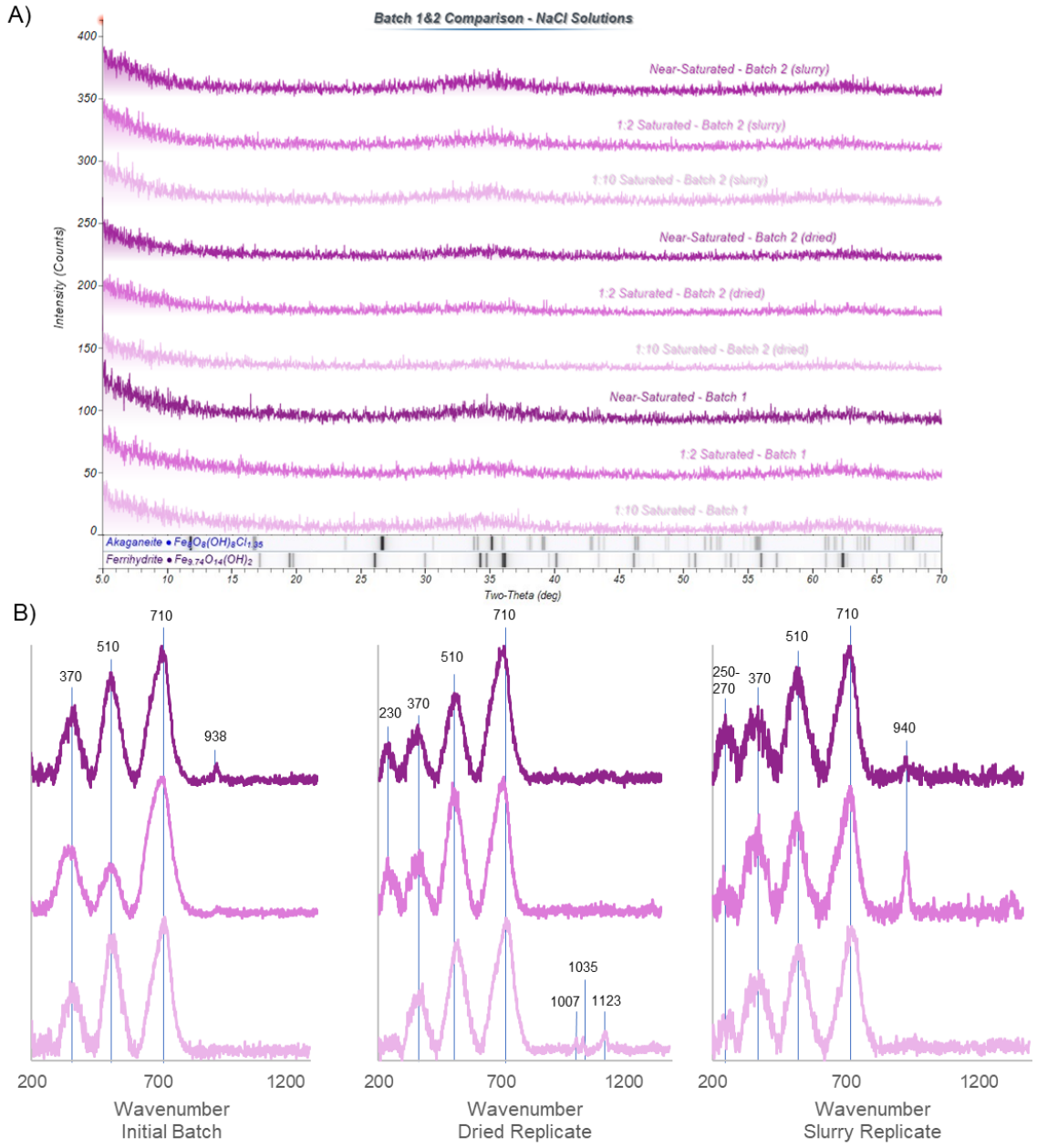

Figure 5: XRD (a) and Raman spectra (b) for NaCl near-saturated (dark purple), 1:2 diluted (purple), and 1:10 diluted (light purple) samples. Raman graphs show the results of each concentration of each batch (initial=left column, dried replicate=middle column, slurry replicate=right column. Values for peaks are given in cm^{-1}. Peaks at 370, 510, and 710 indicate ferrihydrite, 230 is likely hematite, a small peak at 1123 may indicate goethite, and 250-270 closely aligns with values for lepidocrocite. Cl^- does not exhibit Raman spectra, therefore values 938-1123 are not attributed to salt peaks or iron phases.

Figure 6: XRD and Raman Spectra for $CaCl_2$ Samples

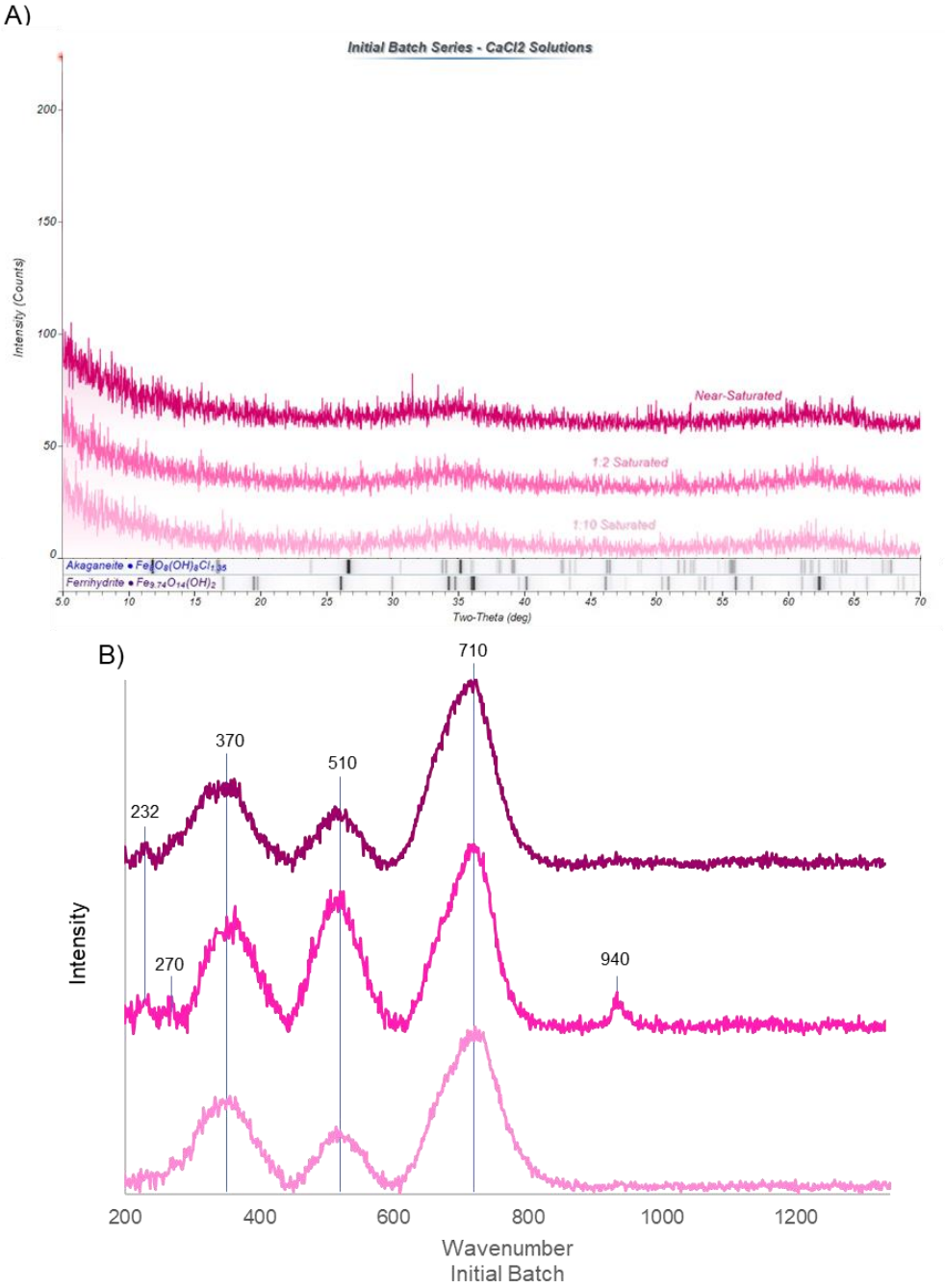

Figure 6: XRD (a) and Raman spectra (b) for $CaCl_2$ near-saturated (dark pink), 1:2 diluted (pink), and 1:10 diluted (light pink) samples. Values for peaks are given in cm^{-1}. Peaks at 370, 510, and 710 indicate ferrihydrite, 230 aligns closely with hematite, and 270 may potentially be lepidocrocite. Red laser power was kept at 0.5% to avoid risk of thermal alteration, but noise was still an issue and exact values for these peaks contain a margin of error. Cl^- does not exhibit Raman spectra, therefore the peak at 940 is not attributed to a salt peak.

Figure 7: XRD and Raman Spectra for $MgCl_2$ Samples

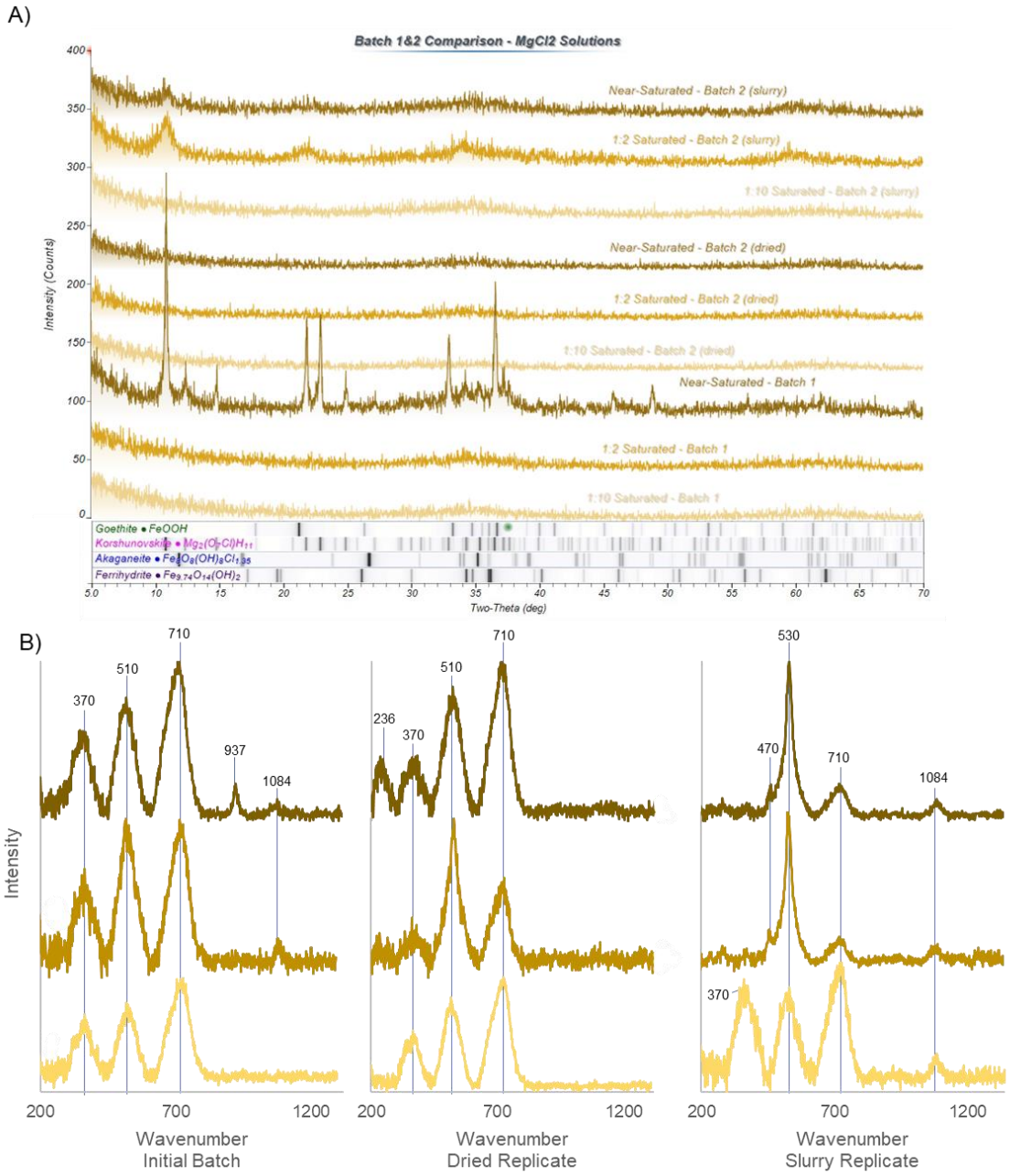

Figure 7: XRD (a) and Raman spectra (b) for $MgCl_2$ near-saturated (dark yellow), 1:2 diluted (yellow), and 1:10 diluted (light yellow) samples. Raman graphs show the results of each concentration of each batch (initial=left column, dried replicate=middle column, slurry replicate=right column. Peaks at 370, 510, and 710 indicate ferrihydrite, 236 closely aligns with goethite, and the unique spectra observed in near-saturated and 1:2 diluted slurry replicates including a peak at 470 is likely the result of Korshunovskite. Values for peaks are given in cm^{-1}. Cl^- does not exhibit Raman spectra, therefore values 937-1084 are not attributed to salt peaks.

Figure 8: XRD and Raman Spectra for $NaNO_3$ Samples

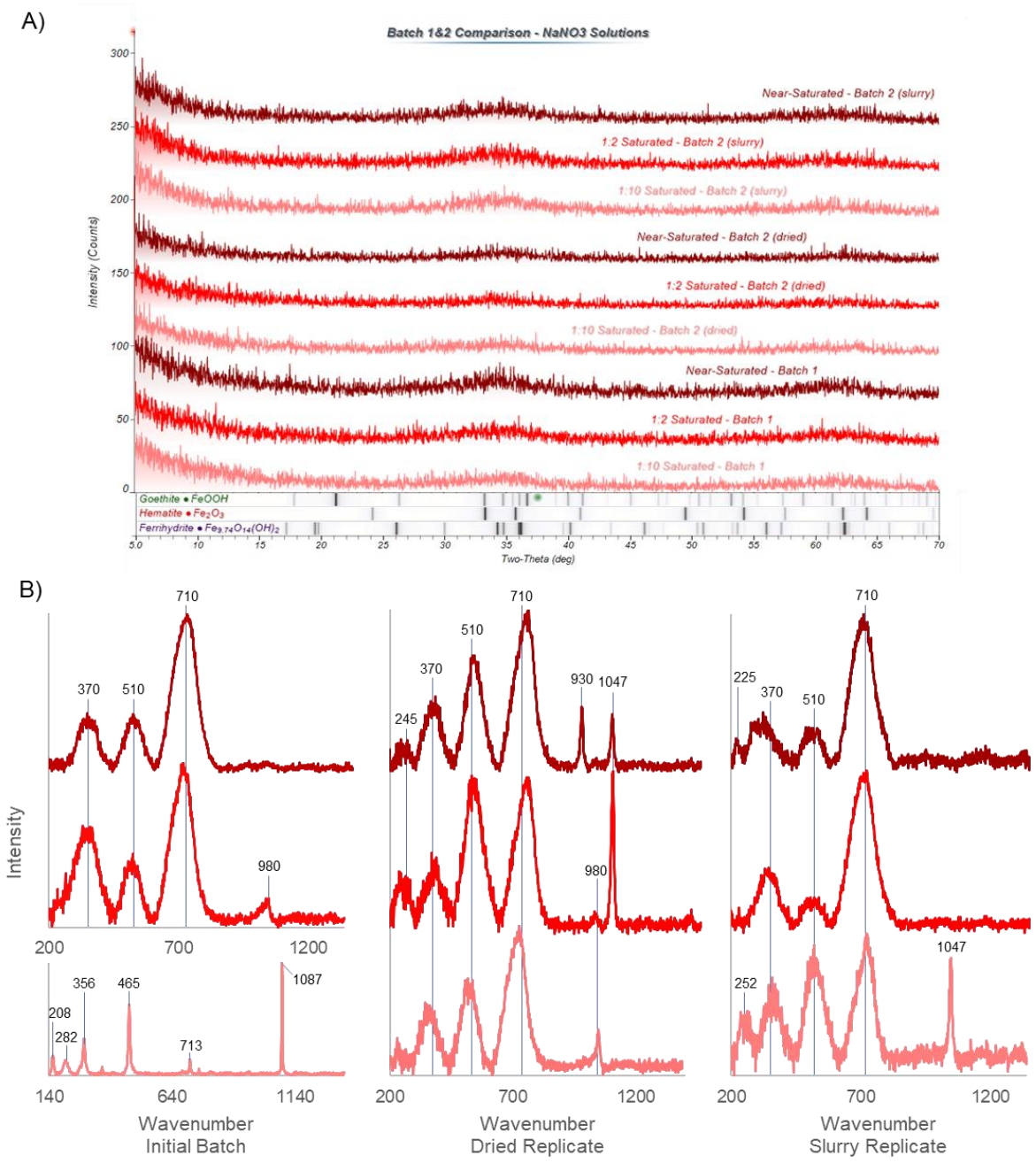

Figure 8: XRD (a) and Raman spectra (b) for $NaNO_3$ near-saturated (dark red), 1:2 diluted (red), and 1:10 diluted (light red) samples. Raman graphs show the results of each concentration of each batch (initial=left column, dried replicate=middle column, slurry replicate=right column. Peaks at 370, 510, and 710 indicate ferrihydrite, lepidocrocite aligns closely with peaks at 208, 252, 282, and 356, 245 matches well with goethite, and 225 matches well with hematite. NO_3^- salt peak is found at ~1049 cm^{-1}.

Figure 9: XRD and Raman Spectra for Na_2CO_3 Samples

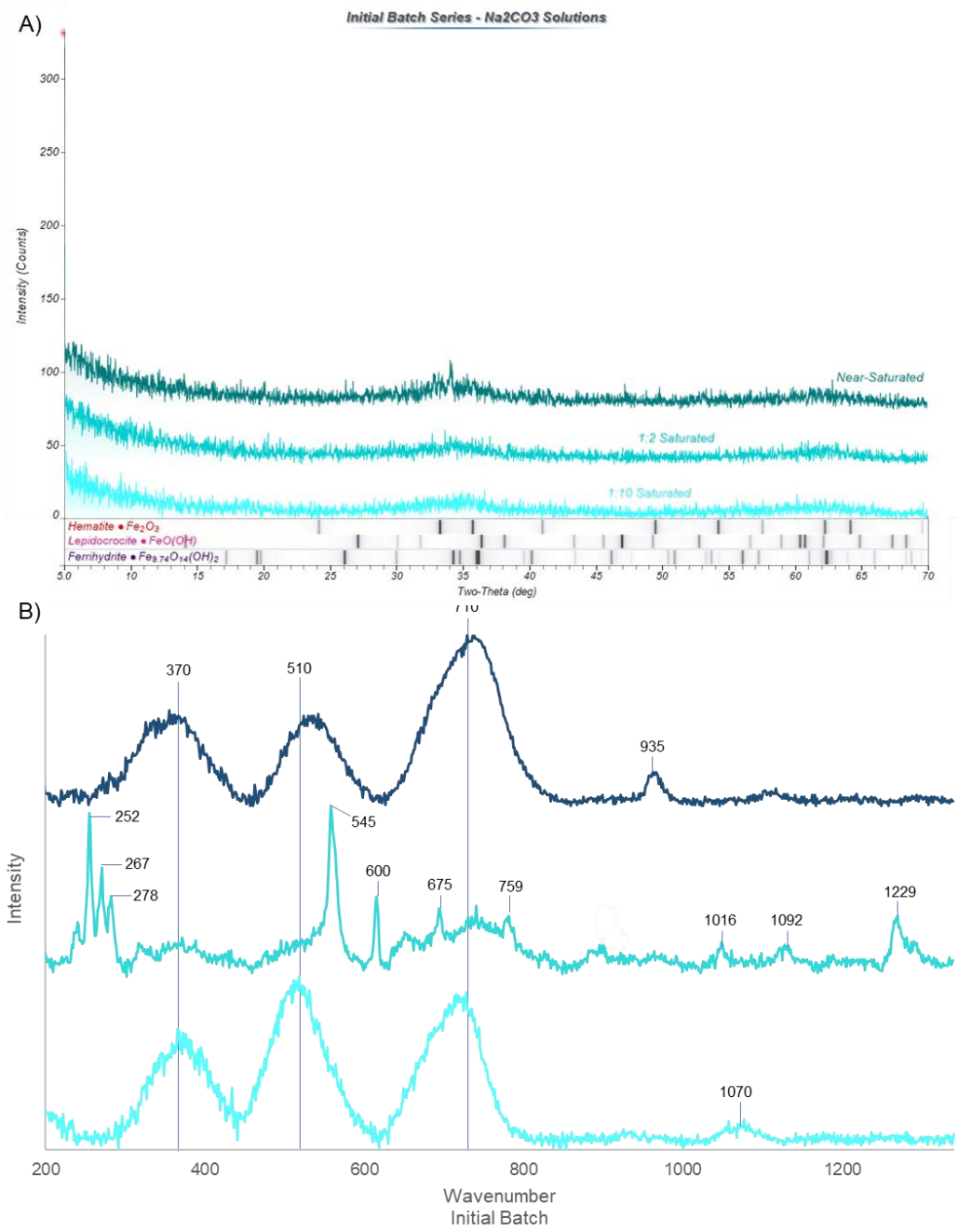

Figure 9: XRD (a) and Raman spectra (b) for Na_2CO_3 near-saturated (dark turquoise), 1:2 diluted (turquoise), and 1:10 diluted (light turquoise) samples. Raman graphs show the results of each concentration of each batch (initial=left column, dried replicate=middle column, slurry replicate=right column. Peaks at 370, 510, and 710 indicate ferrihydrite, 252, 267, and 278 aligns closely with lepidocrocite, 545 aligns closely with goethite, 600 could likely be indicative of hematite, 675 could indicate magnetite, and 1092 may indicate minor amounts of siderite ($FeCO_3$) . CO_3^{2-} salt peak is found at ~1064 cm^{-1}.

Figure 10: XRD and Raman Spectra for Na_2SO_4 Samples

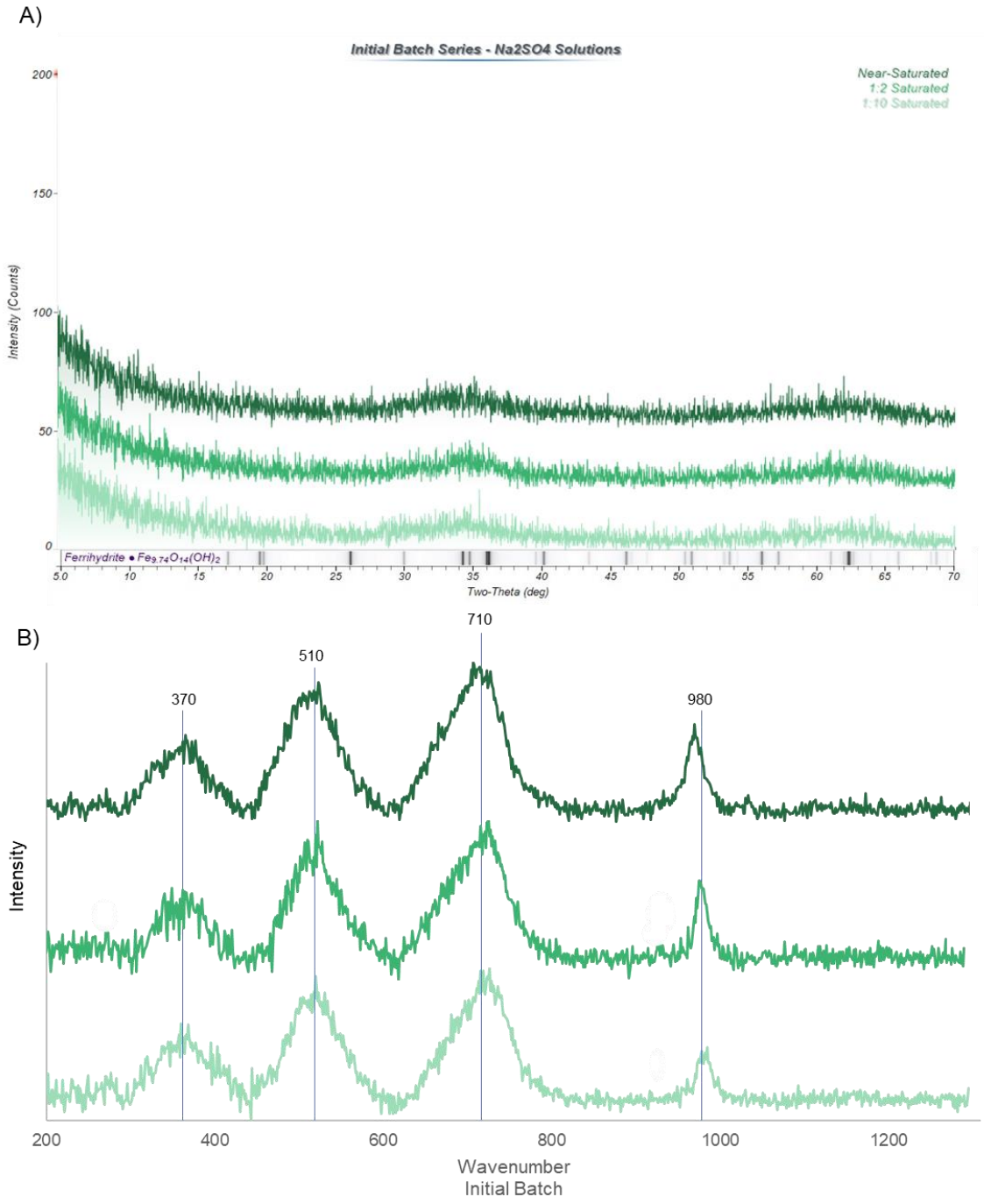

Figure 10: XRD (a) and Raman spectra (b) for Na_2SO_4 near-saturated (dark green), 1:2 diluted (green), and 1:10 diluted (light green) samples. Peaks at 370, 510, and 710 indicate ferrihydrite. SO_4^{2-} salt peak is found at ~980 cm^{-1}.

Figure 11: XRD and Raman Spectra for $NaClO_3$ Samples

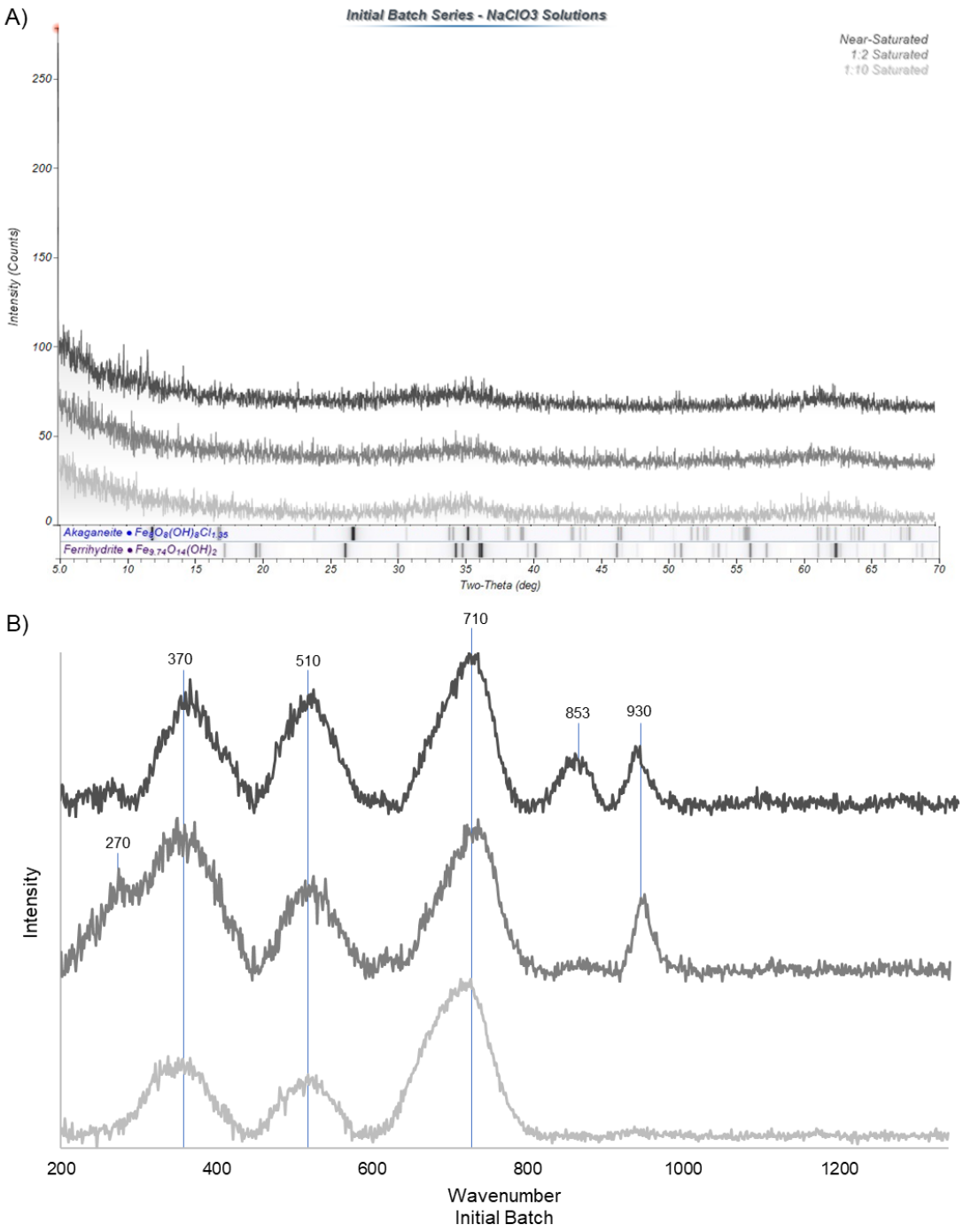

Figure 11: XRD (a) and Raman spectra (b) for $NaClO_3$ near-saturated (dark gray), 1:2 diluted (gray), and 1:10 diluted (light gray) samples. Peaks at 370, 510, and 710 indicate ferrihydrite, 270 closely aligns with values for lepidocrocite. ClO_3^- salt peak is found at ~930 cm^{-1}.

Figure 12: XRD and Raman Spectra for $NaClO_4$ Samples

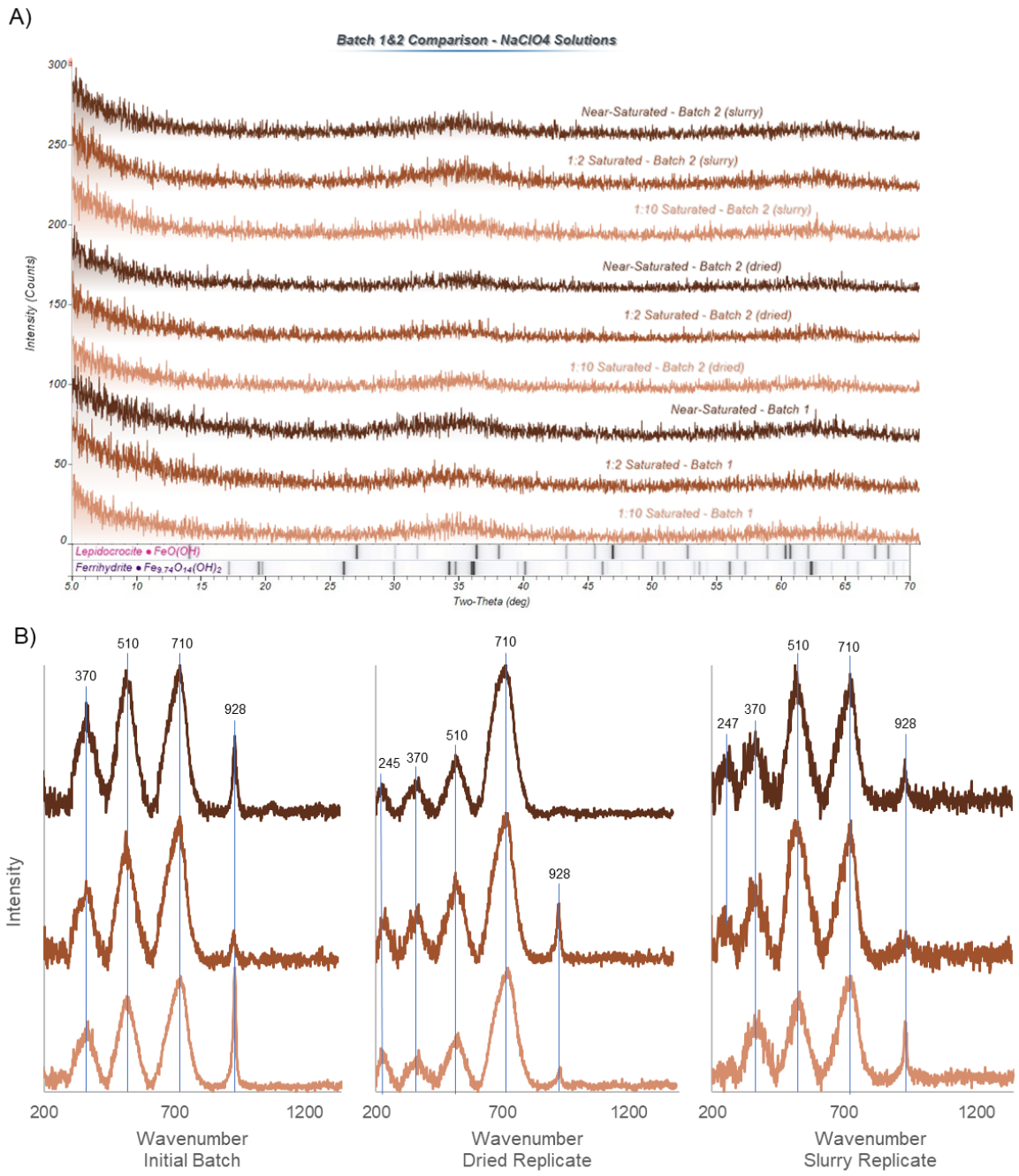

Figure 12: XRD (a) and Raman spectra (b) for $NaClO_4$ near-saturated (dark brown), 1:2 diluted (brown), and 1:10 diluted (light brown) samples. Raman graphs show the results of each concentration of each batch (initial=left column, dried replicate=middle column, slurry replicate=right column. Peaks at 370, 510, and 710 indicate ferrihydrite, and 245-247 is likely indicative of goethite. ClO_4^- salt peak is found at ~928 cm^{-1}.

Figure 13: XRD and Raman Spectra for $MgSO_4$ Samples

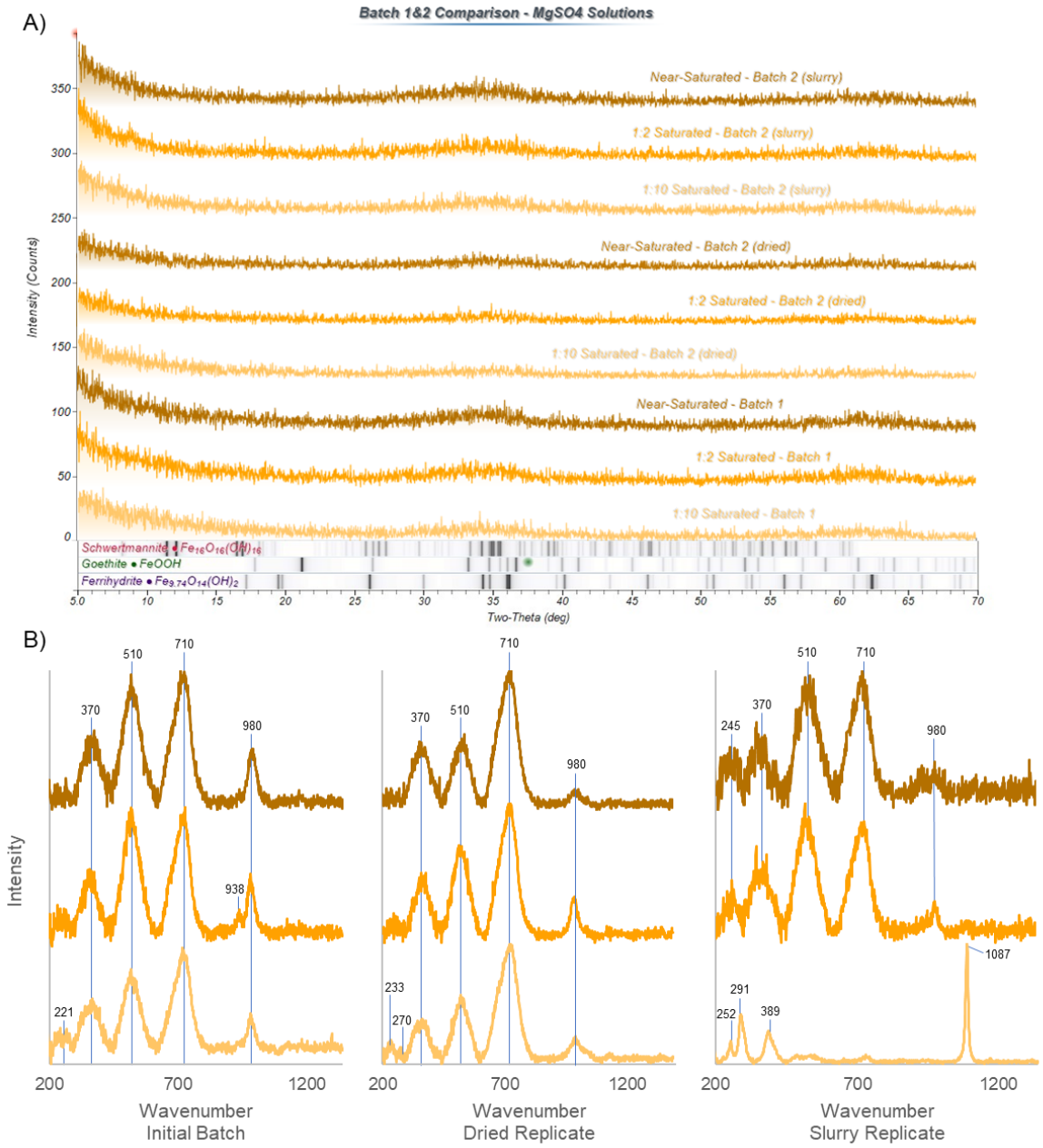

Figure 13: XRD (a) and Raman spectra (b) for $MgSO_4$ near-saturated (dark orange), 1:2 diluted (orange), and 1:10 diluted (light orange) samples. Raman graphs show the results of each concentration of each batch (initial=left column, dried replicate=middle column, slurry replicate=right column. Peaks at 370, 510, and 710 indicate ferrihydrite, 221, 233, and 291 likely indicates hematite, 252 is likely lepidocrocite, and 245 and 389 indicates goethite. SO_4^{2-} salt peak is found at ~980 cm^{-1}.

Table 2: Raman and XRD Peaks for Iron Oxide Phases

Iron Oxide Phase	*Raman Peaks (cm^{-1})*	*XRD Peaks (d-spacings)*	*Source*
Ferrihydrite	370, 510, 710, 1045	2.56, 1.37	Das and Hendry (2011), Hanesch (2009)
Hematite	222, 230, 290, 408, 490, 607	3.50, 2.22, 2.05	
Goethite	162, 243, 297, 384, 447, 545, 665, 1120	4.88, 4.18, 3.37	
Lepidocrocite	140, 214, 249, 284, 345, 374, 524, 647	5.87, 2.91, 2.16, 1.71	
Magnetite	295, 521, 662	2.48, 2.05, 1.26	
Akaganéite	137, 307, 387, 535, 597, 719, 906	7.34, 5.87, 3.12	
Schwertmannite	191, 294, 318, 350, 421, 544, 580, 715, 981	7.34, 3.24, 2.41, 1.87, 1.57, 1.51, 1.32	RRUFF Database, Jade software
Maghemite	350, 512, 665, 730	5.87, 3.37, 2.91, 2.41, 1.57, 4.18, 1.32	Hanesch (2009)

Table 2: Raman and XRD peaks used as reference for identifying ferrihydrite and additional iron oxide phases. Adapted from Das and Hendry (2011), with additional information from Hanesch (2009), RRUFF Database, and Jade peak analysis software.

Table 3: XRD results by wt%

Sample Name	Fer	Goe	Hem	Lep	Mgn	Aka	Sch	Mgh	Korsh
Fh Synthesis 1	100	-	-	-	-	-	-	-	-
Fh Synthesis 2	100	-	-	-	-	-	-	-	-
UPW-B1	10.9	39.8	5.6	-	43.7	-	-	-	-
UPW-B2 (dried)	100	-	-	-	-	-	-	-	-
UPW-B2 (slurry)	1.3	19.6	45.0	-	34.1	-	-	-	-
NS NaCl-B1	15.2	3.3	23.3	-	57.2	-	-	-	-
NS NaCl-B2 (dried)	36.4	3.2	16.5	6.0	17.1	20.9	-	-	-
NS NaCl-B2 (slurry)	-	12.8	15.2	-	72.0	-	-	-	-
1:2 NaCl-B1	43.9	32.0	4.3	-	-	-	-	19.9	-
1:2 NaCl-B2 (dried)	88.4	2.2	2.3	0.9	6.3	-	-	-	-
1:2 NaCl-B2 (slurry)	100	-	-	-	-	-	-	-	-
1:10 NaCl-B1	67.5	1.4	13.2	-	10.3	7.2	-	-	-
1:10 NaCl-B2 (dried)	49.5	-	22.6	3.7	1.2	23.1	-	-	-
1:10 NaCl-B2 (slurry)	46.1	7.1	0.9	-	-	-	-	45.9	-
NS $CaCl_2$	61.8	14.8	-	-	1.5	16.5	-	5.3	-
1:2 $CaCl_2$	48	1.5	11.0	8.8	-	-	-	30.7	-
1:10 $CaCl_2$	56.9	1.4	16.5	-	2.2	-	-	20.9	-
NS $MgCl_2$-B1	3.6	-	-	-	-	-	-	-	96.4
NS $MgCl_2$-B2 (dried)	25.5	13.5	1.8	-	21.5	2.8	-	2.9	32.1
NS $MgCl_2$-B2 (slurry)	3.3	73.9	-	-	-	-	-	-	22.7
1:2 $MgCl_2$-B1	6.7	70.9	-	3.2	18.9	-	-	-	0.3
1:2 $MgCl_2$-B2 (dried)	16.3	72.6	1.6	-	7.6	-	-	-	1.9
1:2 $MgCl_2$-B2 (slurry)	0.2	82.1	-	-	-	-	-	-	17.7

Table 3: XRD results by wt% (cont.)

Sample Name	Fer	Goe	Hem	Lep	Mgn	Aka	Sch	Mgh	Korsh
1:10 $MgCl_2$-B1	62.4	-	3.8	-	-	-	-	25.2	8.6
1:10 $MgCl_2$-B2 (dried)	1.1	1.6	-	-	2.5	-	-	22.7	72.2
1:10 $MgCl_2$-B2 (slurry)	10.7	1.2	3.3	2.3	0.4	-	-	0.7	81.4
NS $NaNO_3$-B1	7.7	2.8	-	-	89.4	-	-	-	-
NS $NaNO_3$-B2 (dried)	10.4	51.3	3.0	3.9	-	-	-	31.4	-
NS $NaNO_3$-B2 (slurry)	29.6	19.7	11.4	-	7.6	-	-	31.7	-
1:2 $NaNO_3$-B1	34.1	4.2	13.3	6.8	3.8	-	-	37.9	-
1:2 $NaNO_3$-B2 (dried)	100	-	-	-	-	-	-	-	-
1:2 $NaNO_3$-B2 (slurry)	-	38.9	26.1	8.4	26.5	-	-	-	-
1:10 $NaNO_3$-B1	6.2	79.5	6.2	8.2	-	-	-	-	-
1:10 $NaNO_3$-B2 (dried)	1.5	73.7	-	-	1.3	-	-	15.3	-
1:10 $NaNO_3$-B2 (slurry)	13.0	32.8	23.3	-	2.9	-	-	-	-
NS $MgSO_4$-B1	100	-	-	-	-	-	-	-	-
NS $MgSO_4$-B2 (dried)	100	-	-	-	-	-	-	-	-
NS $MgSO_4$-B2 (slurry)	100	-	-	-	-	-	-	-	-
1:2 $MgSO_4$-B1	100	-	-	-	-	-	-	-	-
1:2 $MgSO_4$-B2 (dried)	100	-	-	-	-	-	-	-	-
1:2 $MgSO_4$-B2 (slurry)	18.1	-	36.9	-	24.1	-	-	20.9	-

Table 3: XRD results by wt% (cont.)

Sample Name	Fer	Goe	Hem	Lep	Mgn	Aka	Sch	Mgh	Korsh
1:10 $MgSO_4$-B1	22.0	23.7	3.8	6.2	-	-	39.6	4.6	-
1:10 $MgSO_4$-B2 (dried)	66.6	15.2	2.8	-	-	-	-	15.3	-
1:10 $MgSO_4$-B2 (slurry)	86.9	8.2	2.0	-	2.9	-	-	-	-
NS Na_2CO_3	70.6	-	10.8	11.0	7.6	-	-	-	-
1:2 Na_2CO_3	51	7.5	1.0	-	10.3	-	-	30.3	-
1:10 Na_2CO_3	65.0	0.1	9.8	-	-	-	-	25.2	-
NS Na_2SO_4	100	-	-	-	-	-	-	-	-
1:2 Na_2SO_4	100	-	-	-	-	-	-	-	-
1:10 Na_2SO_4	100	-	-	-	-	-	-	-	-
NS $NaClO_3$	20.2	21.3	1.3	1.4	52.1	1.3	-	2.4	-
1:2 $NaClO_3$	43.9	32	4.3	-	-	-	-	19.9	-
1:10 $NaClO_3$	17.5	1.5	39.7	0.7	3.7	-	-	36.5	-
NS $NaClO_4$-B1	100	-	-	-	-	-	-	-	-
NS $NaClO_4$-B2 (dried)	57.9	-	16.4	-	25.8	-	-	-	-
NS $NaClO_4$-B2 (slurry)	-	27.0	6.1	3.2	44.5	-	10.3	8.9	-
1:2 $NaClO_4$-B1	29.4	19.1	32.3	-	4.4	-	-	14.8	-
1:2 $NaClO_4$-B2 (dried)	100	-	-	-	-	-	-	-	-
1:2 $NaClO_4$-B2 (slurry)	-	6.2	25.6	7.5	60.7	-	-	-	-

Sample Name	Fer	Goe	Hem	Lep	Mgn	Aka	Sch	Mgh	Korsh
1:10 $NaClO_4$-B1	90.2	-	7.0	-	1.5	-	-	1.2	-
1:10 $NaClO_4$-B2 (dried)	10.8	9.8	6.4	12.1	60.7	-	-	-	-
1:10 $NaClO_4$-B2 (slurry)	13.8	78.0	7.7	-	-	-	-	0.6	-

Table 3: Results of XRD analysis for initial (B1) and replicate (B2 dried/slurry) brine reaction batches by wt%. Mineral phases are abbreviated as such: ferrihydrite-Fer, goethite-Goe, hematite-Hem, lepidocrocite-Lep, magnetite-Mgn, akaganéite-Aka, schwertmannite-Sch, maghemite-Mgh, korshunovskite-Korsh. Samples without B1/B2 are part of the initial batch series. The results of these calculated wt% are likely inaccurate due to the issues of using MDI-Jade software on the XRD spectra of our samples as previously described.

Table 4: Raman Results

Sample Name	Fer	Goe	Hem	Lep	Mgn	Aka	Sch	Mgh	Korsh
Fh Synthesis 1									
Fh Synthesis 2									
UPW-B1									
UPW-B2 (dried)									
UPW-B2 (slurry)									
NS NaCl-B1									
NS NaCl-B2 (dried)									
NS NaCl-B2 (slurry)									
1:2 NaCl-B1									
1:2 NaCl-B2 (dried)									
1:2 NaCl-B2 (slurry)									
1:10 NaCl-B1									
1:10 NaCl-B2 (dried)									
1:10 NaCl-B2 (slurry)									
NS $CaCl_2$									
1:2 $CaCl_2$									
1:10 $CaCl_2$									
NS $MgCl_2$-B1									
NS $MgCl_2$-B2 (dried)									
NS $MgCl_2$-B2 (slurry)									
1:2 $MgCl_2$-B1									
1:2 $MgCl_2$-B2 (dried)									
1:2 $MgCl_2$-B2 (slurry)									

Table 4: Raman Results (cont.)

Sample Name	Fer	Goe	Hem	Lep	Mgn	Aka	Sch	Mgh	Korsh
1:10 $MgCl_2$-B1									
1:10 $MgCl_2$-B2 (dried)									
1:10 $MgCl_2$-B2 (slurry)									
NS $NaNO_3$-B1									
NS $NaNO_3$-B2 (dried)									
NS $NaNO_3$-B2 (slurry)									
1:2 $NaNO_3$-B1									
1:2 $NaNO_3$-B2 (dried)									
1:2 $NaNO_3$-B2 (slurry)									
1:10 $NaNO_3$-B1									
1:10 $NaNO_3$-B2 (dried)									
1:10 $NaNO_3$-B2 (slurry)									
NS $MgSO_4$-B1									
NS $MgSO_4$-B2 (dried)									
NS $MgSO_4$-B2 (slurry)									
1:2 $MgSO_4$-B1									

Sample Name	Fer	Goe	Hem	Lep	Mgn	Aka	Sch	Mgh	Korsh
1:2 $MgSO_4$-B2 (dried)									
1:2 $MgSO_4$-B2 (slurry)									
1:10 $MgSO_4$-B1									
1:10 $MgSO_4$-B2 (dried)									
1:10 $MgSO_4$-B2 (slurry)									
NS Na_2CO_3									
1:2 Na_2CO_3									
1:10 Na_2CO_3									
NS Na_2SO_4									
1:2 Na_2SO_4									
1:10 Na_2SO_4									
NS $NaClO_3$									
1:2 $NaClO_3$									
1:10 $NaClO_3$									
NS $NaClO_4$-B1									
NS $NaClO_4$-B2 (dried)									
NS $NaClO_4$-B2 (slurry)									
1:2 $NaClO_4$-B1									
1:2 $NaClO_4$-B2 (dried)									
1:2 $NaClO_4$-B2 (slurry)									

Sample Name	Fer	Goe	Hem	Lep	Mgn	Aka	Sch	Mgh	Korsh
1:10 $NaClO_4$-B1									
1:10 $NaClO_4$-B2 (dried)									
1:10 $NaClO_4$-B2 (slurry)									

Table 4: Results of phases detected by Raman spectroscopy for each brine type and saturation level. Dominant phases detected are shaded with black, residual phases are shaded with medium gray, and minor phases are shaded with light gray. B1 = batch 1 (freeze-dried), B2 = batch 2, either freeze-dried or slurry.

Figure 14: SEM Images of Dried Ferrihydrite + Salt Precipitates

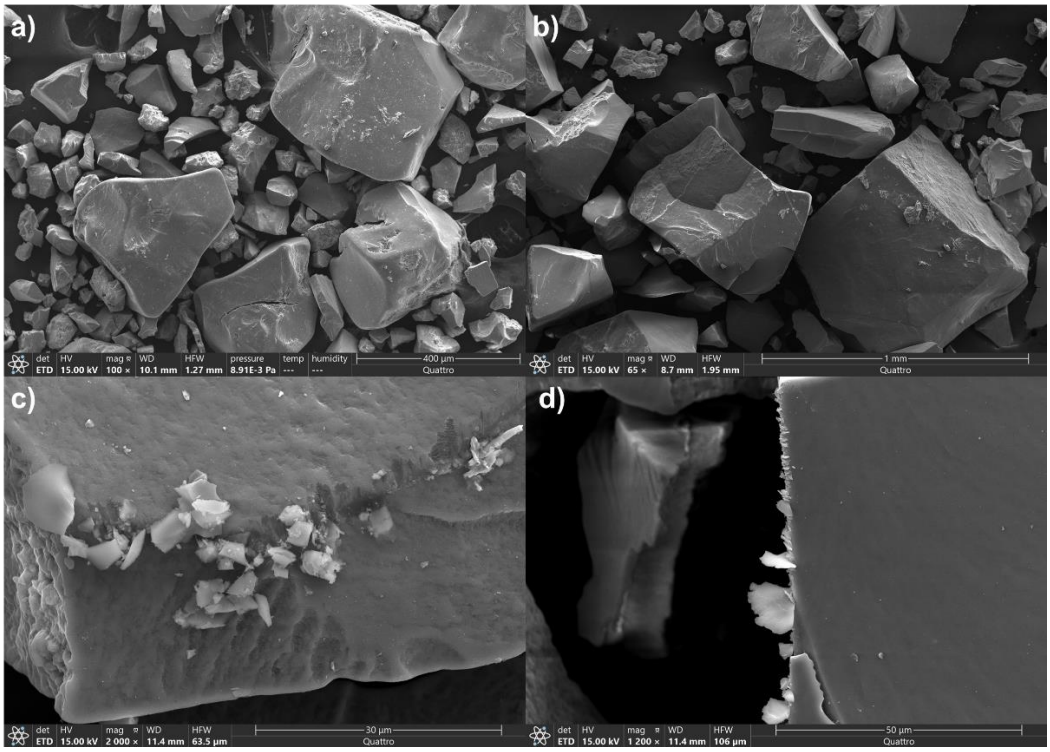

Figure 10: SEM secondary electron images of reacted ferrihydrite samples from (a) UPW, (b) near-saturated $MgSO_4$, (c) 1:2 saturated NaCl, and (d) 1:2 saturated Na_2SO_4 at 15 kV. 10a and b show the particle sizes of ferrihydrite that resulted from freeze-drying prior to mixing in solution where particle size had a significant range, and 10 c and d show examples of salt precipitating on the edges of ferrihydrite grains and the likely result for strong salt peaks detected in Raman spectroscopy.

Figure 15: SEM Images of Spherules Found

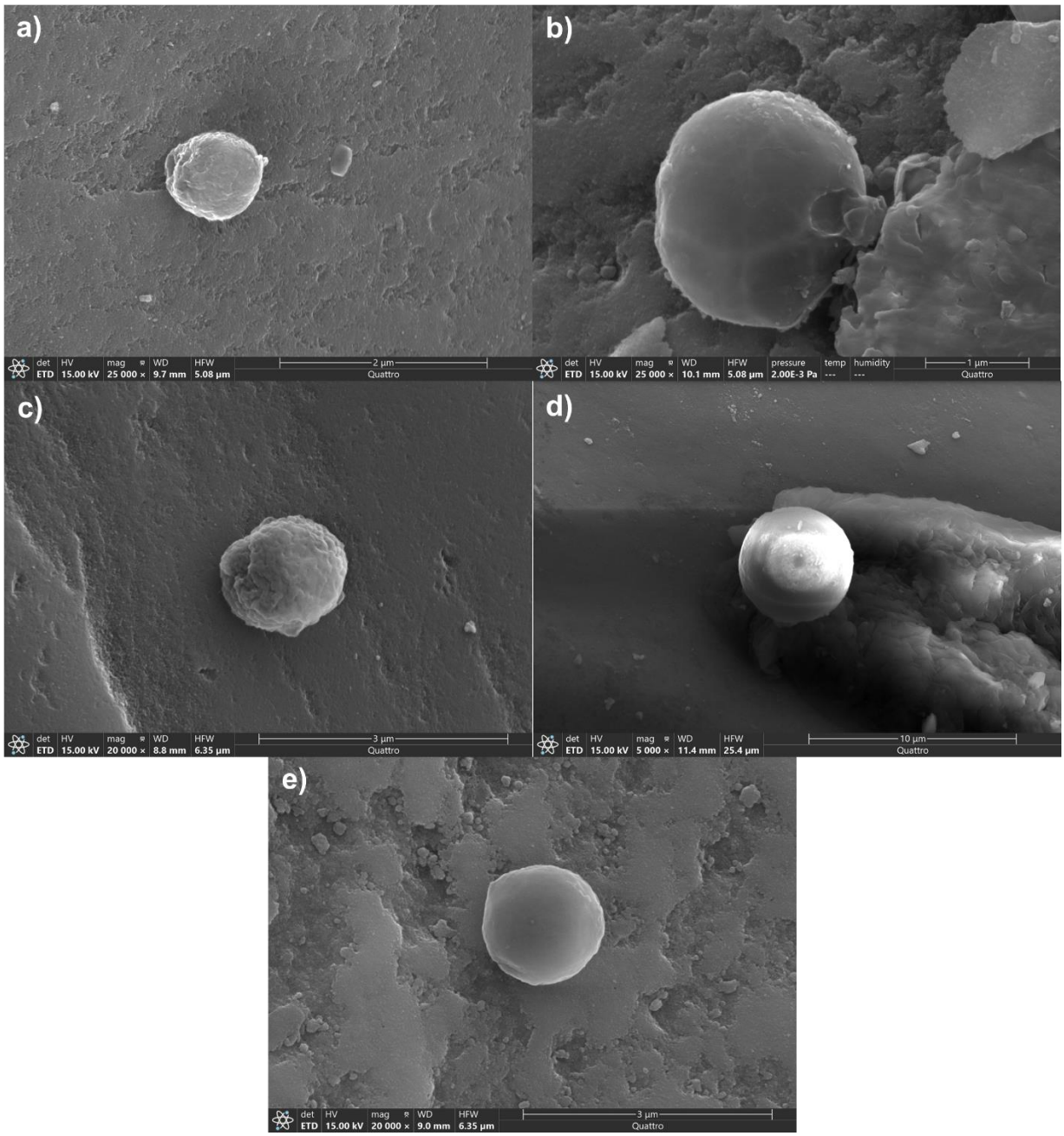

Figure 11: SEM secondary electron imaging of spherical particles located in near-saturated (a) NaCl, (b) $NaNO_3$, (c) $MgSO_4$, and (d) 1:2 saturated Na_2SO_4 and (e) $MgSO_4$. Magnification ranges from 5000-25000x at 15 kV.

Figure 16: SEM Image of Long Needle-like Structure from 1:10 saturated $NaNO_3$

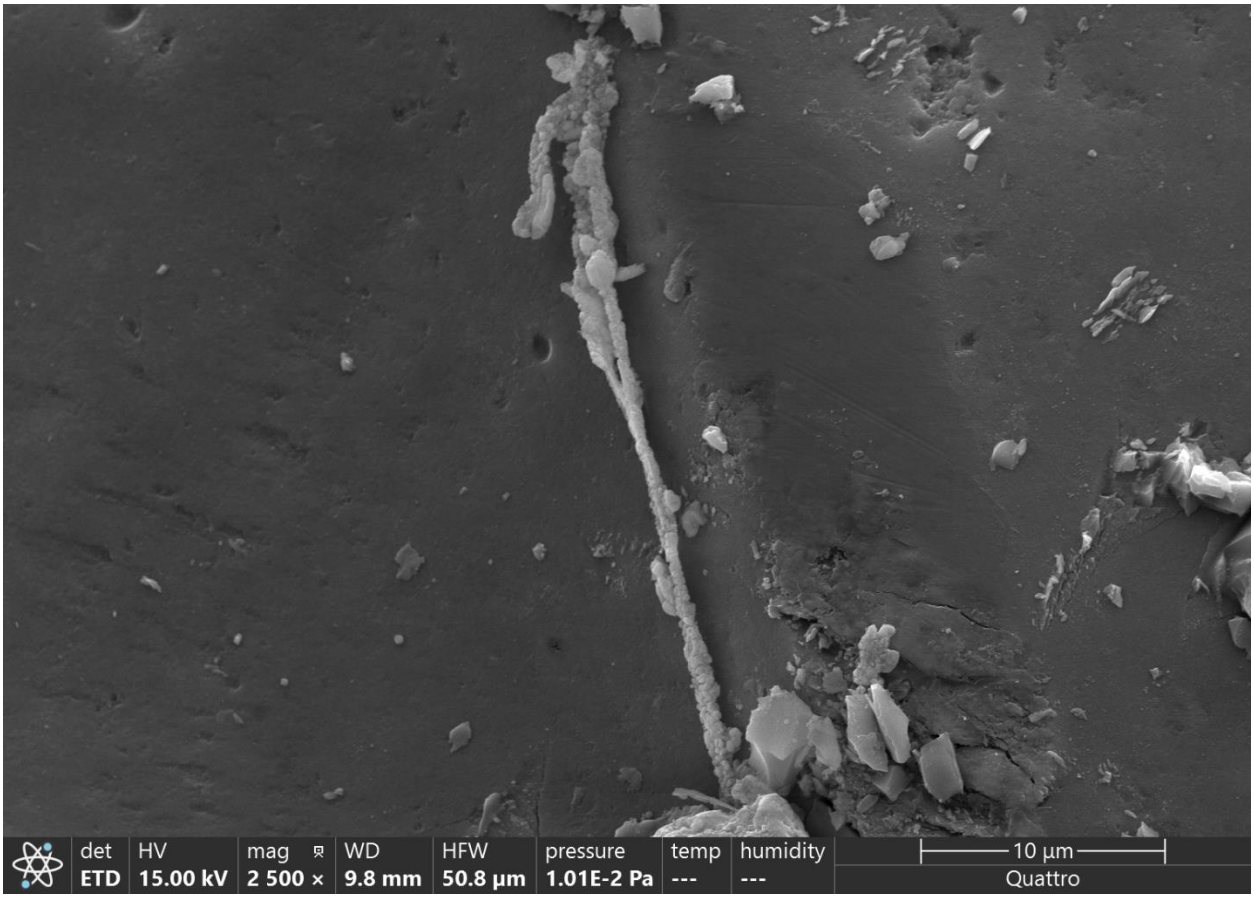

Figure 12: SEM secondary image at 2500x and 15 kV of needle-like particle found on the surface of a ferrihydrite grain.

Figure 17: SEM Images of Slurry Ferrihydrite Particles and Dissolution Pits

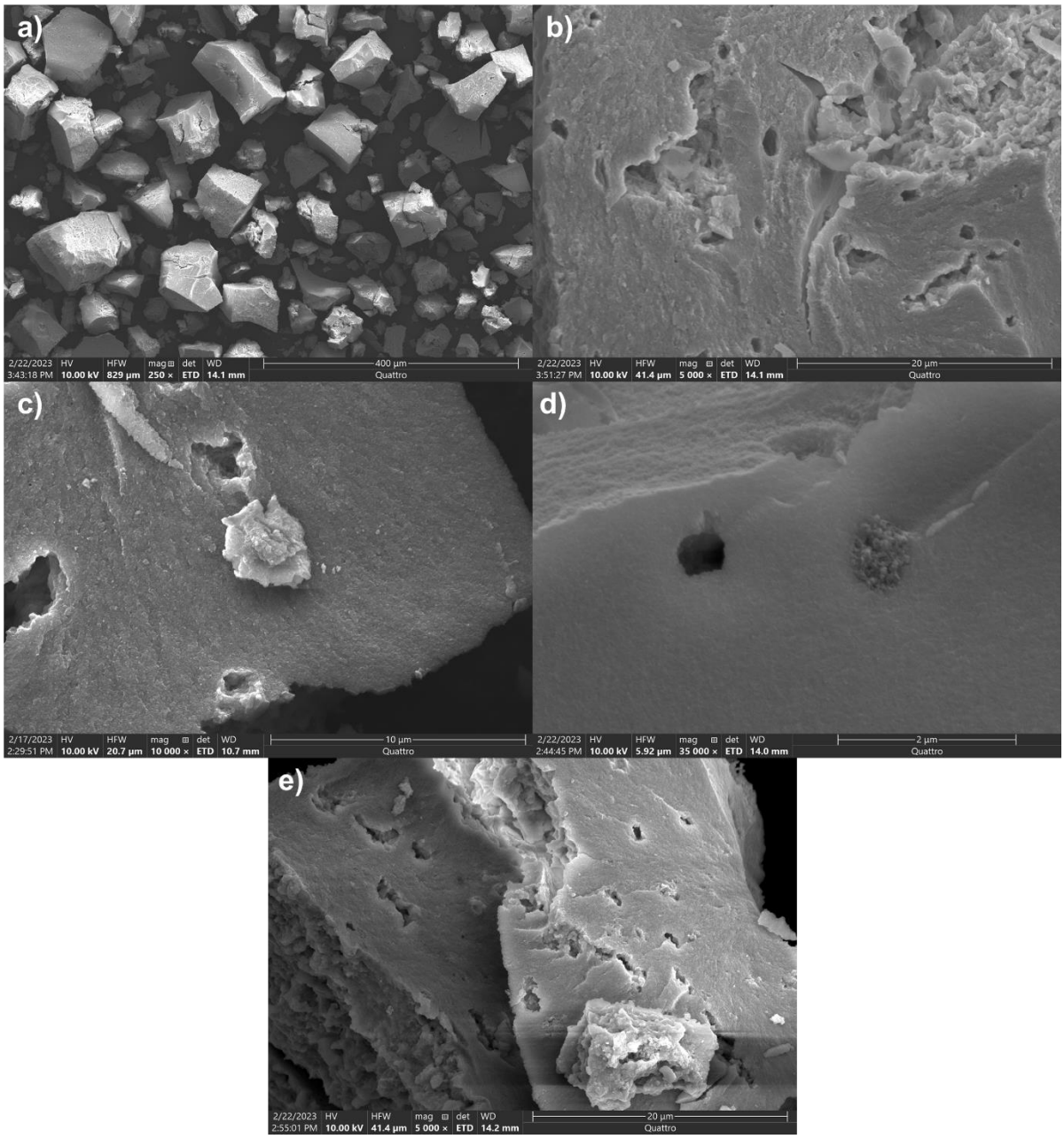

Figure 13: SEM secondary electron images of ferrihydrite slurry particle sizes from (a) UPW, and the appearance of dissolution pits on larger ferrihydrite grains from (b) UPW, (c) 1:10 saturated $NaClO_4$, (d) 1:2 saturated $NaNO_3$, and (e) near-saturated $NaNO_3$. The largest particles observed in slurry samples were 100 µm in diameter, compared to 400-600 µm in the dried samples. Dissolution pits appeared in several samples, and seemed to be both vacant and occupied with precipitation of new iron oxide phases.

Figure 18: SEM Images of Ferrihydrite Reacted with Near-Saturated $MgSO_4$

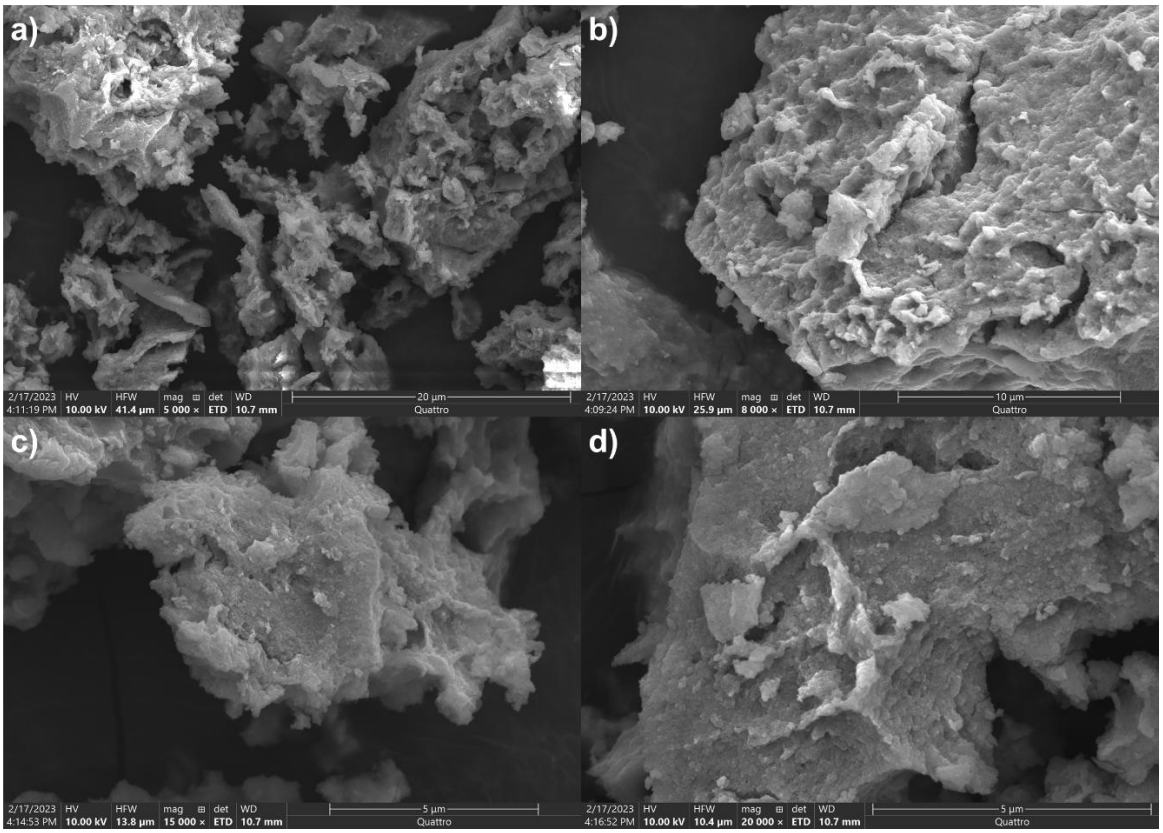

Figure 14: SEM secondary electron images of ferrihydrite slurry reacted with near-saturated $MgSO_4$ at (a) 5000x, (b) 8000x, (c) 15,000x, and (d) 20,000x. Surface textures of these aggregates show a greater degree of alteration compared to those observed in the dried experimental sets. Aggregate size was also smaller on average compared to the dried experimental sets.

Figure 19: SEM Images of Ferrihydrite Reacted with $MgCl_2$ Solutions

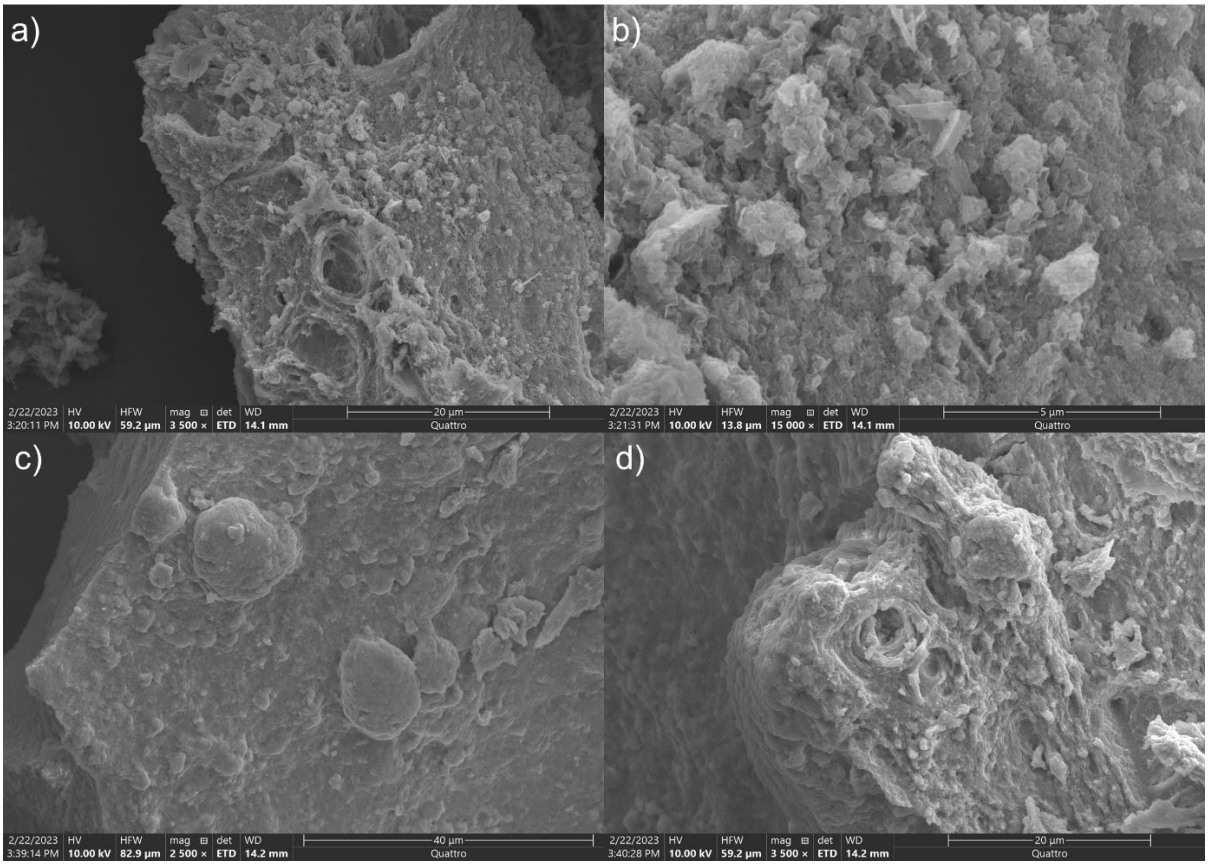

Figure 15: SEM secondary electron images of ferrihydrite slurry reacted with (a and b) 1:2 saturated and (c and d) near-saturated $MgCl_2$ at 10.00 kV. Both solutions showed particles with significantly altered surfaces and dissolution pits. Small korshunovskite particles (prismatic) can also be seen easily in a and b.

Figure 20: SEM Images of Larger Spherules

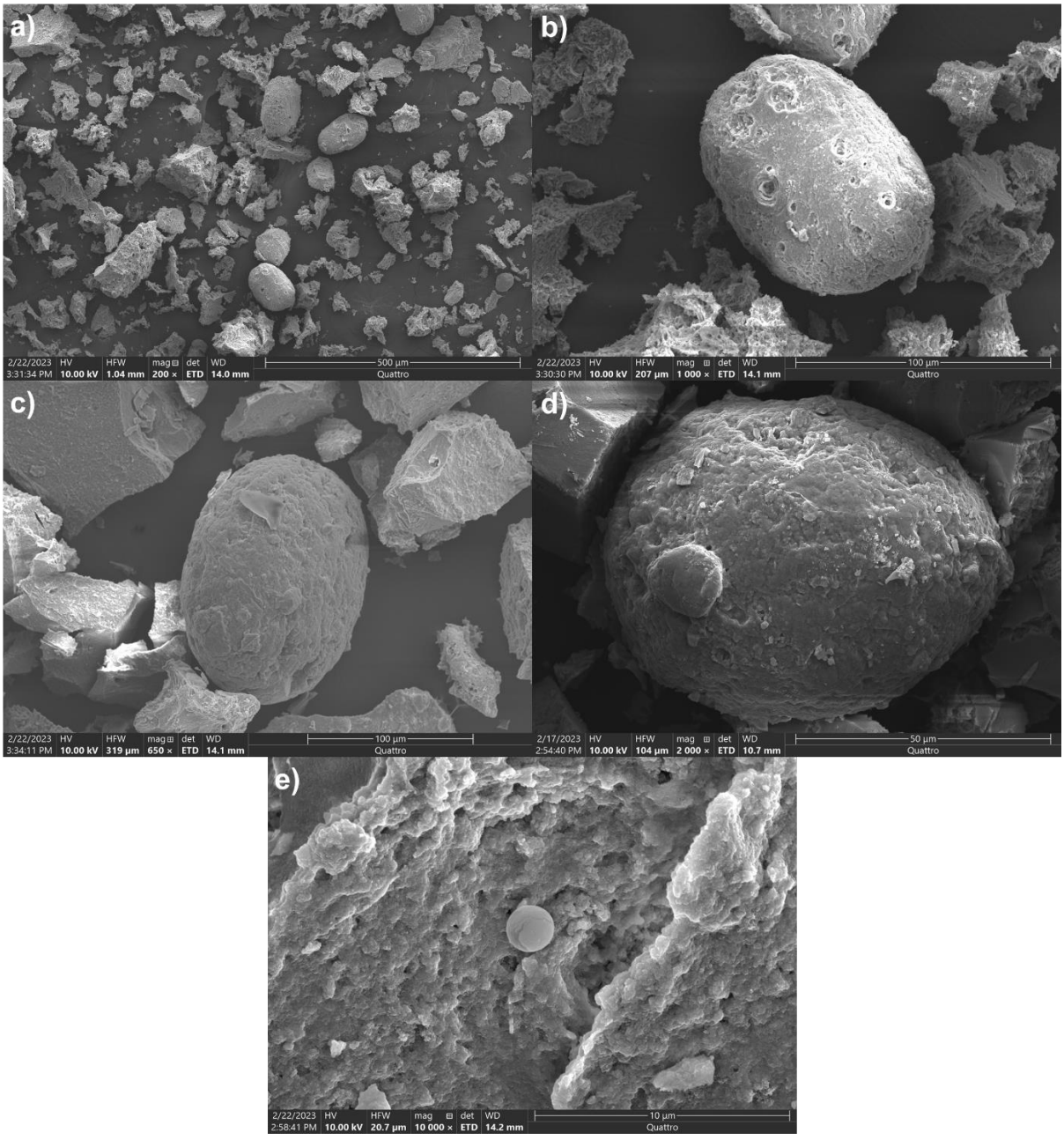

Figure 16: SEM secondary electron images of large, oblong shaped particles found in (a and b) 1:2 saturated and (c) near-saturated $MgCl_2$, and (d) 1:2 saturated $NaClO_4$. These particles resembled the smaller spherical particles such as one found in (e) near-saturated $NaNO_3$ and those from Figure 11, but were significantly larger in size reaching a diameter of 100 µm.

Figure 21: TEM Image of Ferrihydrite Slurry

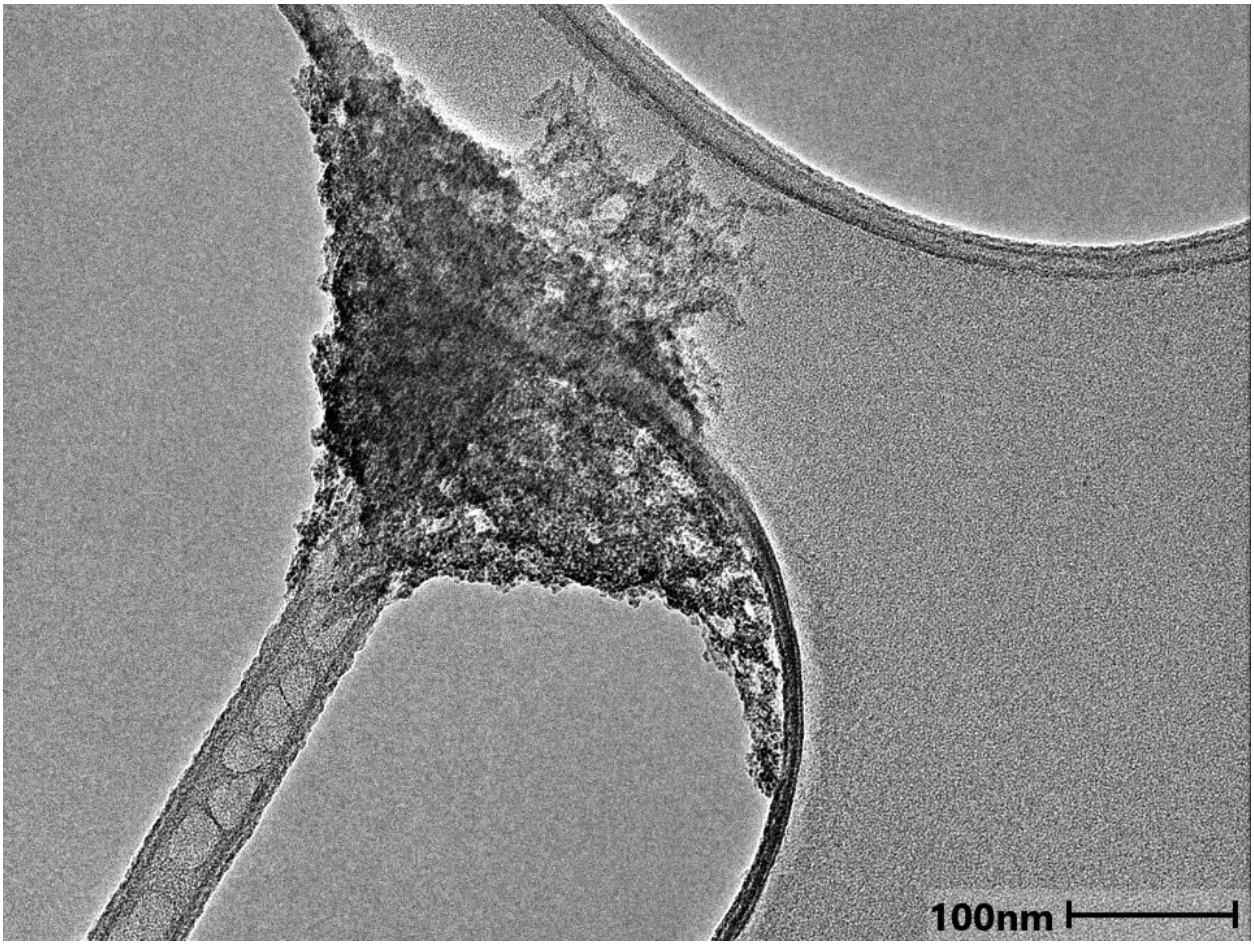

Figure 21: Unreacted ferrihydrite slurry imaged at 30,000x. Electron diffraction of this sample showed that ferrihydrite slurry exhibits very poor crystallinity, bordering amorphous.

Figure 22: TEM Images of 1:2 diluted and Near-Saturated $MgCl_2$ Samples

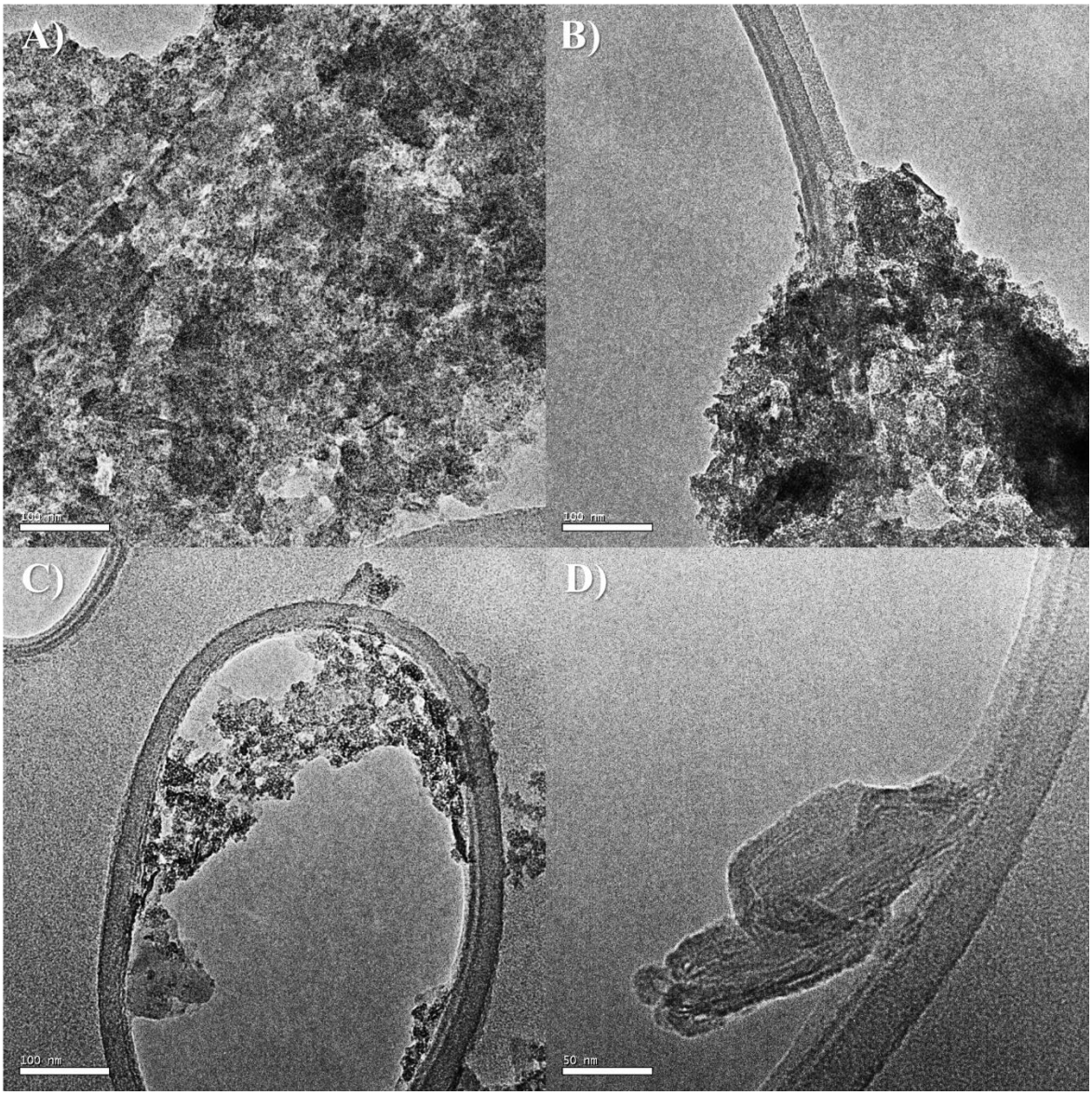

Figure 22: TEM images of slurry replicate samples filtered from (a and b) near-saturated $MgCl_2$ at 30,000x, and 1:2 diluted $MgCl_2$ at (c) 30,000x and (d) 60,000x.

Table 5: pH Changes for Initial Batch

Salt Type	*Saturation*	*Initial pH*	*Final pH*	*Change in pH*
UPW	-	6.06	4.56	-1.50
NaCl	1:10	8.82	6.72	-2.10
	1:2	9.03	6.86	-2.17
	Near-Sat.	9.22	6.18	-3.04
$NaNO_3$	1:10	6.10	6.31	+0.21
	1:2	5.87	7.29	+1.42
	Near-Sat.	5.78	8.48	+2.70
Na_2CO_3	1:10	11.53	11.80	+0.27
	1:2	11.39	11.60	+0.41
	Near-Sat.	11.30	11.51	+0.21
Na_2SO_4	1:10	8.15	7.01	-1.14
	1:2	8.30	6.87	-1.43
	Near-Sat.	8.71	8.96	+0.25
$NaClO_3$	1:10	6.18	9.24	+3.06
	1:2	6.12	9.05	+2.93
	Near-Sat.	6.51	9.27	+2.76
$NaClO_4$	1:10	7.62	9.44	+1.82
	1:2	7.96	9.01	+1.05
	Near-Sat.	8.26	8.38	+0.12
$CaCl_2$	1:10	6.50	7.55	+1.05
	1:2	5.56	4.79	-0.77
	Near-Sat.	4.54	4.95	+0.41
$MgCl_2$	1:10	9.37	8.06	-1.31
	1:2	6.71	7.77	+1.06
	Near-Sat.	6.17	6.12	-0.05
$MgSO_4$	1:10	8.55	6.43	-2.12
	1:2	8.25	7.14	-1.11
	Near-Sat.	7.58	7.05	-0.53

Table 5: Initial and final pH results for initial batch reaction series by salt type and saturation level.

Table 6: pH Changes for Dried Replicate Batch

Salt Types	*Saturation*	*Initial pH*	*Final pH*	*Change in pH*
UPW	-	6.12	3.91	-2.21
NaCl	1:10	6.90	6.81	-0.09
	1:2	6.38	6.19	-0.19
	Near-sat.	6.94	7.23	+0.29
NaNO3	1:10	5.53	6.57	+1.04
	1:2	5.50	5.84	+0.34
	Near-sat.	5.39	5.67	+0.28
NaClO4	1:10	8.90	5.87	-3.03
	1:2	8.75	6.07	-2.68
	Near-sat.	8.23	5.49	-2.74
MgCl2	1:10	9.34	6.85	-2.49
	1:2	7.74	7.04	-0.70
	Near-sat.	6.00	5.88	-0.12
$MgSO_4$	1:10	8.80	6.43	-2.37
	1:2	8.57	6.97	-1.60
	Near-sat.	7.98	6.78	-1.20

Table 6: Initial and final pH results for dried replicate batches by salt type and saturation level.

Table 7: pH Changes for Slurry Replicate Batch

Salt Type	*Saturation*	*Initial pH*	*Final pH*	*Change in pH*
UPW	-	6.08	4.83	-1.25
NaCl	1:10	8.05	6.51	-1.54
	1:2	6.50	6.44	-0.06
	Near-sat.	6.37	5.98	-0.39
$NaNO_3$	1:10	5.76	6.84	+1.08
	1:2	5.71	5.97	+0.26
	Near-sat.	5.48	5.56	+0.08
$NaClO_4$	1:10	8.67	6.57	-2.10
	1:2	8.72	6.82	-1.90
	Near-sat.	7.77	5.70	-2.07
$MgCl_2$	1:10	9.33	7.83	-1.50
	1:2	7.72	6.63	-1.09
	Near-sat.	5.98	5.90	-0.08
$MgSO_4$	1:10	8.77	6.54	-2.23
	1:2	8.60	7.14	-1.46
	Near-sat.	8.16	7.14	-1.02

Table 7: Initial and final pH results for slurry replicate batches by salt type and saturation level.

Figure 23: Brine Chemistry Diagram for Ferrihydrite Transformation Pathways

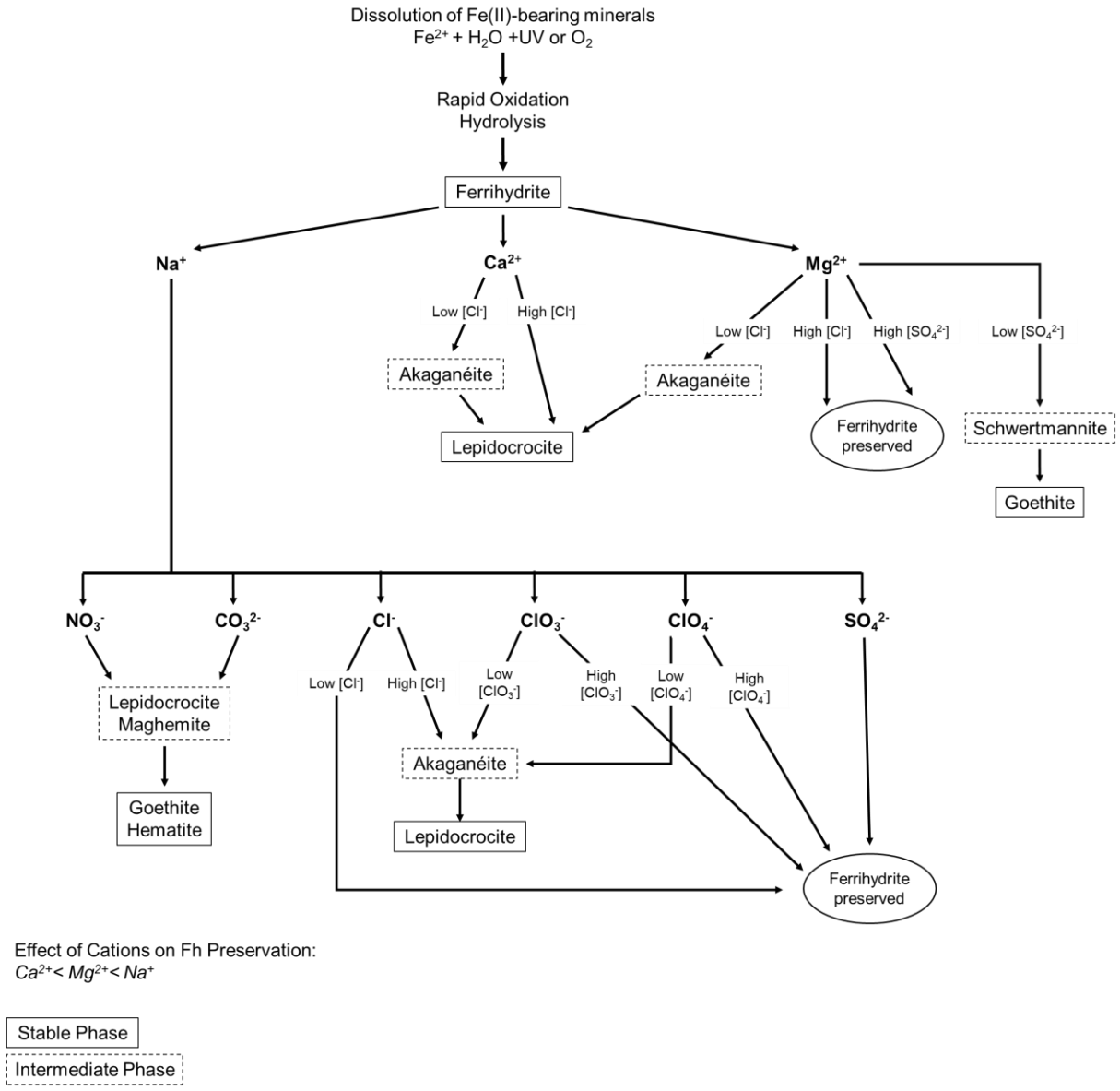

Figure 23: The proposed flowchart of ferrihydrite dissolution and transformation pathways, dependent on cation and anion chemistry of a given brine solution. This diagram is based primarily on observations of transformation products made using Raman spectroscopy.

REFERENCES

Arinchtein, A., Schmack, R., Kraffert, K., Radnik, J., Dietrich, P., Sachse, R., & Kraehnert, R. (2020). Role of Water in Phase Transformations and Crystallization of Ferrihydrite and Hematite. *ACS Applied Materials & Interfaces*, *12*(34), 38714–38722. https://doi.org/10.1021/acsami.0c05253

Barron, V., Torrent, J., & Greenwood, J. (2006). Transformation of jarosite to hematite in simulated Martian brines. *Earth and Planetary Science Letters*, *251*(3–4), 380–385. https://doi.org/10.1016/j.epsl.2006.09.022

Bell, J. F., Maki, J. N., Alwmark, S., Ehlmann, B. L., Fagents, S. A., Grotzinger, J. P., Gupta, S., Hayes, A., Herkenhoff, K. E., Horgan, B. H. N., Johnson, J. R., Kinch, K. B., Lemmon, M. T., Madsen, M. B., Núñez, J. I., Paar, G., Rice, M., Rice, J. W., Schmitz, N., … Yingling, R. (2022). Geological, multispectral, and meteorological imaging results from the Mars 2020 Perseverance rover in Jezero crater. *Science Advances*, *8*(47), eabo4856. https://doi.org/10.1126/sciadv.abo4856

Berger, Jeff A., Schmidt, Mariek E., Gellert, Ralf, Campbell, John L., & King, Penelope L. (2016). A global Mars dust composition refined by the Alpha-Particle X-ray Spectrometer in Gale Crater. *Geophysical Research Letters*, *43*, 67–75. https://doi.org/10.1002/2015GL066675.

Bibring, J.-P., Arvidson, R. E., Gendrin, A., Gondet, B., Langevin, Y., Le Mouelic, S., Mangold, N., Morris, R. V., Mustard, J. F., Poulet, F., Quantin, C., & Sotin, C. (2007). Coupled Ferric Oxides and Sulfates on the Martian Surface. *Science*, *317*(5842), 1206–1210. https://doi.org/10.1126/science.1144174

Brass, G. W. (1980). Stability of brines on Mars. *Icarus*, *42*(1), 20–28. https://doi.org/10.1016/0019-1035(80)90237-7

Burleson, D. J., & Penn, R. L. (2006). Two-Step Growth of Goethite from Ferrihydrite. *Langmuir*, *22*(1), 402–409. https://doi.org/10.1021/la051883g

Chevrier, V. F., & Rivera-Valentin, E. G. (2012). Formation of recurring slope lineae by liquid brines on present-day Mars: LIQUID BRINES ON MARS. *Geophysical Research Letters*, *39*(21), n/a-n/a. https://doi.org/10.1029/2012GL054119

Clark & Van Hart. (1980). The Salts of Mars. *Icarus*, *45*, 370–378.

Cornell, R. M., & Schwertmann, U. (2003). *The Iron Oxides: Structure, Properties, Reactions, Occurrences, and Uses*. 694.

Cudennec, Y., & Lecerf, A. (2006). The transformation of ferrihydrite into goethite or hematite, revisited. *Journal of Solid State Chemistry*, *179*(3), 716–722. https://doi.org/10.1016/j.jssc.2005.11.030

Cullen, M. D., Phillips-Lander, C. M., Elwood Madden, A. S., & Elwood Madden, M. E. (2021). Siderite Dissolution in Mars-analog Brines: Kinetics and Reaction Products. *The Planetary Science Journal*, *2*(5), 169. https://doi.org/10.3847/PSJ/ac13a3

Das, S., & Hendry, M. J. (2011). Application of Raman spectroscopy to identify iron minerals commonly found in mine wastes. *Chemical Geology*, *290*(3–4), 101–108. https://doi.org/10.1016/j.chemgeo.2011.09.001

Das, S., Hendry, M. J., & Essilfie-Dughan, J. (2011). Transformation of Two-Line Ferrihydrite to Goethite and Hematite as a Function of pH and Temperature. *Environmental Science & Technology*, *45*(1), 268–275. https://doi.org/10.1021/es101903y

Day, M., & Dorn, T. (2019). Wind in Jezero Crater, Mars. *Geophysical Research Letters*, *46*(6), 3099–3107. https://doi.org/10.1029/2019GL082218

Dehouck, E., McLennan, S. M., Sklute, E. C., & Dyar, M. D. (2017). Stability and fate of ferrihydrite during episodes of water/rock interactions on early Mars: An experimental approach: Stability of Ferrihydrite on Early Mars. *Journal of Geophysical Research: Planets*, *122*(2), 358–382. https://doi.org/10.1002/2016JE005222

Elwood Madden, M. E., Madden, A. S., Rimstidt, J. D., Zahrai, S., Kendall, M. R., & Miller, M. A. (2012). Jarosite dissolution rates and nanoscale mineralogy. *Geochimica et Cosmochimica Acta*, *91*, 306–321. https://doi.org/10.1016/j.gca.2012.05.001

Glotch, T. D., & Kraft, M. D. (2008). Thermal transformations of akaganéite and lepidocrocite to hematite: Assessment of possible precursors to Martian crystalline hematite. *Physics and Chemistry of Minerals*, *35*(10), 569–581. https://doi.org/10.1007/s00269-008-0249-z

Golden, D. C., Ming, D. W., Morris, R. V., & Graff, T. G. (2008). Hydrothermal synthesis of hematite spherules and jarosite: Implications for diagenesis and hematite spherule formation in sulfate outcrops at Meridiani Planum, Mars. *American Mineralogist*, *93*(8–9), 1201–1214. https://doi.org/10.2138/am.2008.2737

Hanesch, M. (2009). Raman spectroscopy of iron oxides and (oxy)hydroxides at low laser power and possible applications in environmental magnetic studies. *Geophysical Journal International*, *177*(3), 941–948. https://doi.org/10.1111/j.1365-246X.2009.04122.x

Heaney, P. J., Oxman, M. J., & Chen, S. A. (2020). A structural study of size-dependent lattice variation: In situ X-ray diffraction of the growth of goethite nanoparticles from 2-line ferrihydrite. *American Mineralogist*, *105*(5), 652–663. https://doi.org/10.2138/am-2020-7217

Huminicki, D. M. C., & Rimstidt, J. D. (2009). Iron oxyhydroxide coating of pyrite for acid mine drainage control. *Applied Geochemistry*, *24*(9), 1626–1634. https://doi.org/10.1016/j.apgeochem.2009.04.032

Jiang, Z., Liu, Q., Roberts, A. P., Barrón, V., Torrent, J., & Zhang, Q. (2018). A new model for transformation of ferrihydrite to hematite in soils and sediments. *Geology*. https://doi.org/10.1130/G45386.1

Legett, C., Pritchett, B. N., Elwood Madden, A. S., Phillips-Lander, C. M., & Elwood Madden, M. E. (2018). Jarosite dissolution rates in perchlorate brine. *Icarus*, *301*, 189–195. https://doi.org/10.1016/j.icarus.2017.06.031

Lemmon, M. T., Smith, M. D., Viudez-Moreiras, D., de la Torre-Juarez, M., Vicente-Retortillo, A., Munguira, A., Sanchez-Lavega, A., Hueso, R., Martinez, G., Chide, B., Sullivan, R., Toledo, D., Tamppari, L., Bertrand, T., Bell, J. F., Newman, C., Baker, M., Banfield, D., Rodriguez-Manfredi, J. A., … Apestigue, V. (2022). Dust, Sand, and Winds Within an Active Martian Storm in Jezero Crater. *Geophysical Research Letters*, *49*(17). https://doi.org/10.1029/2022GL100126

Leshin, L. A., & Vicenzi, E. (2006). Aqueous Processes Recorded by Martian Meteorites: Analyzing Martian Water on Earth. *Elements*, *2*(3), 157–162. https://doi.org/10.2113/gselements.2.3.157

Liu, H., Guo, H., Li, P., & Wei, Y. (2008). The transformation of ferrihydrite in the presence of trace Fe(II): The effect of the anionic media. *Journal of Solid State Chemistry*, *181*(10), 2666–2671. https://doi.org/10.1016/j.jssc.2008.06.052

Malinko, S. V. (1983). Korshunovskite $Mg_2Cl(OH)_3 \cdot nH_2O$ a new hydrous magnesium chloride. *International Geology Review*, *25*(9), 1105–1110. https://doi.org/10.1080/00206818309466808

Mazzetti, L., & Thistlethwaite, P. J. (2002). Raman spectra and thermal transformations of ferrihydrite and schwertmannite. *Journal of Raman Spectroscopy*, *33*(2), 104–111. https://doi.org/10.1002/jrs.830

Mianping, Z., Weigang, K., Xuefei, Z., Wenxi, C., & Fanjing, K. (2013). A Comparative Analysis of Evaporate Sediments on Earth and Mars: Implications for the Climate Change on Mars. *Acta Geologica Sinica - English Edition*, *87*(3), 885–897. https://doi.org/10.1111/1755-6724.12096

Mills, S. J., Nestola, F., Kahlenberg, V., Christy, A. G., Hejny, C., & Redhammer, G. J. (2013). Looking for jarosite on Mars: The low-temperature crystal structure of jarosite. *American Mineralogist*, *98*(11–12), 1966–1971. https://doi.org/10.2138/am.2013.4587

Möhlmann, D., & Thomsen, K. (2011). Properties of cryobrines on Mars. *Icarus*, *212*(1), 123–130. https://doi.org/10.1016/j.icarus.2010.11.025

Navrotsky, A., Mazeina, L., & Majzlan, J. (2008). Size-Driven Structural and Thermodynamic Complexity in Iron Oxides. *Science*, *319*(5870), 1635–1638. https://doi.org/10.1126/science.1148614

Osterloo, M. M., Hamilton, V. E., Bandfield, J. L., Glotch, T. D., Baldridge, A. M., Christensen, P. R., Tornabene, L. L., & Anderson, F. S. (2008). Chloride-Bearing Materials in the Southern Highlands of Mars. *Science*, *319*(5870), 1651–1654. https://doi.org/10.1126/science.1150690

Phillips-Lander, C. M., Elwood Madden, A. S., Hausrath, E. M., & Elwood Madden, M. E. (2019). Aqueous alteration of pyroxene in sulfate, chloride, and perchlorate brines: Implications for post-Noachian aqueous alteration on Mars. *Geochimica et Cosmochimica Acta*, *257*, 336–353. https://doi.org/10.1016/j.gca.2019.05.006

Pritchett, B. N., Elwood Madden, M. E., & Madden, A. S. (2012). Jarosite dissolution rates and maximum lifetimes in high salinity brines: Implications for Earth and Mars. *Earth and Planetary Science Letters*, *357–358*, 327–336. https://doi.org/10.1016/j.epsl.2012.09.011

Rivera-Valentín, E. G., Chevrier, V. F., Soto, A., & Martínez, G. (2020). Distribution and habitability of (meta)stable brines on present-day Mars. *Nature Astronomy*, *4*(8), 756–761. https://doi.org/10.1038/s41550-020-1080-9

Sears, D. W. G., & Chittenden, J. D. (2005). On laboratory simulation and the temperature dependence of the evaporation rate of brine on Mars. *Geophysical Research Letters*, *32*(23), L23203. https://doi.org/10.1029/2005GL024154

Sefton-Nash, E., & Catling, D. (2008). Hematitic concretions at Meridiani Planum, Mars: Their growth timescale and possible relationship with iron sulfates. *Earth and Planetary Science Letters*, *269*(3–4), 366–376. https://doi.org/10.1016/j.epsl.2008.02.009

Sidhu, P. S. (1981). Dissolution of Iron Oxides and Oxyhydroxides in Hydrochloric and Perchloric Acids. *Clays and Clay Minerals*, *29*(4), 269–276. https://doi.org/10.1346/CCMN.1981.0290404

Thomas, N. H., Ehlmann, B. L., Meslin, P. -Y., Rapin, W., Anderson, D. E., Rivera-Hernández, F., Forni, O., Schröder, S., Cousin, A., Mangold, N., Gellert, R., Gasnault, O., & Wiens, R. C. (2019). Mars Science Laboratory Observations of Chloride Salts in Gale Crater, Mars. *Geophysical Research Letters*, *46*(19), 10754–10763. https://doi.org/10.1029/2019GL082764

Toner, J. D., Catling, D. C., & Light, B. (2014). Soluble salts at the Phoenix Lander site, Mars: A reanalysis of the Wet Chemistry Laboratory data. *Geochimica et Cosmochimica Acta*, *136*, 142–168. https://doi.org/10.1016/j.gca.2014.03.030

Tosca, N. J., & McLennan, S. M. (2006). Chemical divides and evaporite assemblages on Mars. *Earth and Planetary Science Letters*, *241*(1–2), 21–31. https://doi.org/10.1016/j.epsl.2005.10.021

Zahrai, S. K., Elwood Madden, M. E., Madden, A. S., & Rimstidt, J. D. (2013). Na-jarosite dissolution rates: The effect of mineral composition on jarosite lifetimes. *Icarus*, *223*(1), 438–443. https://doi.org/10.1016/j.icarus.2012.12.020

Appendix A:

Batch	$Fe(NO_3)_3$ mass (g)	Water added (mL)	Initial pH	KOH added (mL)	Final pH
Test Batch	20.2	491.9	1.61	170.2	7.10
1	20.2	491.9	1.66	190.2	7.04
2	40.4	983.8	1.64	379	7.39
3	40.4	1000	1.65	377	7.25
4	20.2	491.9	1.62	189.5	7.17

Table A1: Values for 2-line ferrihydrite synthesis from $Fe(NO_3)_3 \cdot 9H_2O$. Batches 2 and 3 were doubled in quantity while maintaining a pH range of 7-8. In this procedure, pH is determined to be the critical factor in achieving the above chemical reaction.